Available online at www.sciencedirect.com
ScienceDirect
Journal of Sound and Vibration 307 (2007) 428–451
JOURNAL OF SOUND AND VIBRATION
www.elsevier.com/locate/jsvi

Quantification of clearance-induced impulsive sources in a torsional system

Ashley R. Crowther, Carrie Janello, Rajendra Singh*

Acoustics and Dynamics Laboratory, Mechanical Engineering Department, The Ohio State University, 201 West 19th Ave, Columbus, OH 43210, USA

Received 1 September 2005; received in revised form 22 December 2006; accepted 9 May 2007
Available online 21 August 2007

Abstract

The impulse response problem in a multi-degree-of-freedom torsional system with multiple clearances is examined with focus on the quantification of the source. This system is related to a vehicle driveline and a map of external transient torque excitations is defined within the operating range of an internal combustion engine. Nonlinear transient solutions are found numerically for the entire excitation map. Proposed metrics include a global metric that indicates the number and nature of impacts, metrics measured just before impact, the relative kinetic energy and relative acceleration of impacting bodies and metrics measured just after impact, initial torque rise, initial velocity rise, peak to peak acceleration and time-windowed mean-square acceleration. Phase plane analysis is applied to explain the differences between the magnitudes of impulses for impact types, illustrating that the relative acceleration between impacting bodies and the relative kinetic energy determine the impact severity. Analysis shows that the metrics measured after impact correlate well. Nonetheless, using numerical or experimental data sets for systems with multiple clearances, it is demonstrated that the windowed mean-square acceleration metric permits an 'energy' calculation with multiple impact events that could be either isolated or combined. Chief contributions of this research include better quantification and an understanding of impulsive sources that arise during rapid changes in external torque excitations.

1. Introduction

Many torsional components have clearances necessitated by their function, such as within gears, splines and joints. Fig. 1a provides a generic example of a torsional system, where linear sub-systems are coupled via nonlinear elastic elements (Fig. 1b). Impacts may occur when external torque, shown in Fig. 1a as $T_e(t)$, changes drastically and the subsequent angular motions pass quickly through the clearance(s) in the torque–angular displacement relationship of Fig. 1b. This could lead to impulsive responses or vibro-impacts that could manifest themselves into the following three classes of problems, depending on the nature of excitation: gear rattle, gear whine with tooth separation and transient impacts. In 2003, Wang et al. [1] surveyed about 200 papers covering the existing literature on the first two problems, without mentioning

*Corresponding author. Tel.: +1 614 292 4147; fax: +1 614 292 3163.
E-mail address: singh.3@osu.edu (R. Singh).

0022-460X/$ - see front matter © 2007 Elsevier Ltd. All rights reserved.
doi:10.1016/j.jsv.2007.05.055

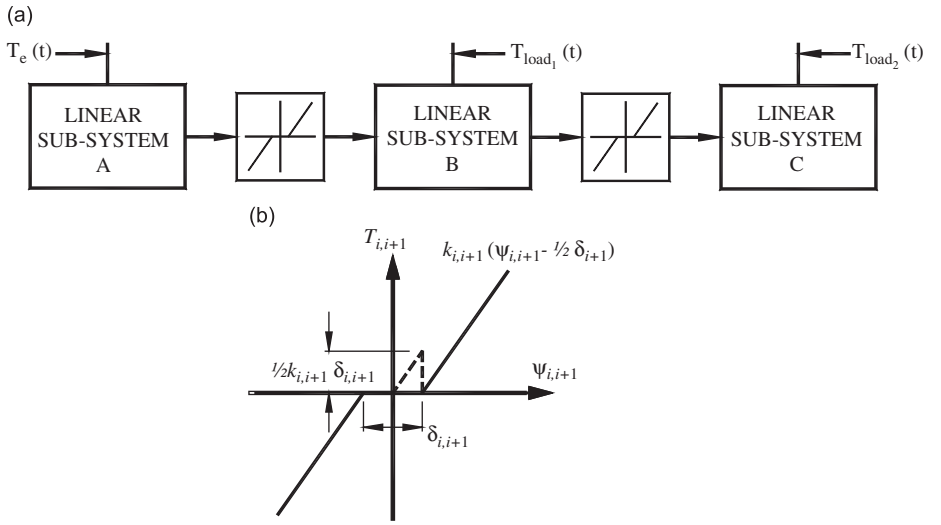

Fig. 1. (a) Generic torsional system subject to transient torque excitations. Here the linear sub-systems A, B and C are joined by the piecewise nonlinear springs characterized in (b).

transient impacts, where the literature is sparse. For the sake of illustration, the motivation of our work is related to vehicle powertrains where the resulting impulsive noise is known as 'clunk'. Such torsional systems exhibit many clearances and the components whose impacts have the highest amount of energy seem to dominate this noise source [2]. In a recent article [3], we demonstrated the formulation, simulation and provided experimental correlation for the nonlinear transient response. Further, Oh and Singh [4] proposed four impulsive source metrics for this problem: instantaneous speed change at impact, peak to peak torsional acceleration, peak amplitude of the interfacial torque within the gear pair and the nature and number of impacts. However, only limited cases were studied for the effects of certain parameters on the impulsive events.

The understanding of dynamic responses for systems with clearances is important from the standpoint of noise, vibration, and stress and fatigue analyses. Mechanisms including pin and ball joints [5,6] and gear pairs [7] and simple piecewise nonlinear oscillators [8] have been examined. Further, in Ref. [3] a detailed review is provided for literature related to the vehicle driveline clunk. As a prelude to our research several books [9–12] on impact mechanisms were examined but none address the type of problem that is specifically examined in this paper. Further, only a few articles have proposed and examined metrics for some impulsive motions in geared systems, such as Refs. [2,4,13]. In addition to Oh and Singh [4], Padmanabhan and Singh [13] proposed four source metrics, including a metric based on the energy within the initial sharp pulse of duration, Δt. In Ref. [2], a subjective clunk evaluation was reported for a manual transmission with two objectionable qualities found; the 'metallic clanging' and multiple impacts events. In this paper, we examine the fundamentals of the impulse response problem using a generic torsional system with a clearance-type nonlinearity that could describe a family of driveline systems. We intend to evaluate new and existing impulsive event metrics and compare their effectiveness in quantifying the clearance-induced source strength. Various attributes of the behavior including phase planes are studied over an illustrative range of transient (ramp-down) torque excitations.

2. Problem formulation

2.1. Scope, objectives and assumptions

The generic system of Fig. 1a, with linear sub-systems and multiple clearances is used to formulate Fig. 2, which represents one possible configuration for automotive driveline systems. The homogeneous (unforced) system is linear until contacting bodies pass through their clearance. Then linear sub-systems would be

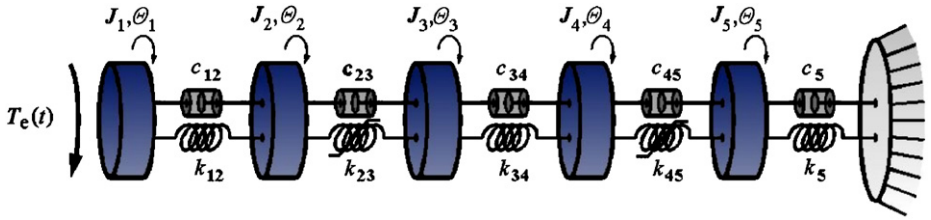

Fig. 2. Five degree-of-freedom model of the generic torsional system. Here the elements k_{23} and k_{45} have been designated as typical locations for clearance. Parameters are: $J_1 = 0.2$, $J_2 = 0.05$, $J_3 = 0.008$, $J_4 = 0.0158$, $J_5 = 0.05\,(\mathrm{kg\,m^2})$, $k_{12} = 7180$, $k_{23} = 323000$, $k_{34} = 102000$, $k_{45} = 450000$, $k_5 = 1400\,(\mathrm{N\,m/rad})$, $C_{12} = 0.15$, $C_{23} = 0.1$, $C_{34} = 2.2$, $C_{45} = 3.5$, $C_5 = 2.95\,(\mathrm{N\,m\,s/rad})$.

connected by piecewise elastic elements. Natural modes of the corresponding linear system vary depending on sub-system separation(s), e.g. the grouping A, B and C, in Fig. 1a, represents the case of both stiffness elements k_{23} and k_{45} in clearance, as in Fig. 2. Typically, in vehicle powertrains, impacts result from vibrational response at the lowest mode due to a transient engine excitation [14]. Rapid change in initial rigid body twist (mean load) and/or in braking conditions may play a role [15]. In this paper, we focus only on the engine excitation, $T_e(t)$, shown in Fig. 2, that is comprised of initial, T_m and transient, ΔT_m, parts. Previously a smoothened ramp-type function was suggested as a reasonable representation for torque ramp up/down [3]. However, for the specific case of evaluation of metrics, a non-smoothened ramp-type transient may be assumed, with initial torques and ramp up/down components. The chief objectives are as follows: (1) formulate a generic torsional system with one or two clearances based on the knowledge of automotive driveline systems; (2) conduct nonlinear simulations under transient excitations and develop new or refined metrics for the impulsive source; (3) evaluate and compare selected quantifiers over a map of transient excitations using surface and line plots; (4) construct the typical phase-plane diagrams for impulsive responses and further understand the behavior of transient impacts. It should be noted that the following clearance nonlinearity issues or methods have been omitted in our study: (a) impact damping [16–17], (b) smoothening for the discontinuous transition in the piecewise clearance function [18] and (c) non-dimensionalization of key parameters to aid with the numerical stiffness problem [19].

2.2. Torsional model of the linear system

The torsional motions of the model presented in Fig. 2 are described by angular displacements, $\theta_i(t)$, where $i = 1,2,\ldots,5$. The equations of motion for the corresponding linear system (assuming no clearance) are:

$$\mathbf{J}\ddot{\boldsymbol{\theta}} + C\dot{\boldsymbol{\theta}} + \mathbf{K}(\theta)\boldsymbol{\theta}(t) = \mathbf{T}(t,\theta), \tag{1}$$

where J_i, represents the component inertias, $k_{i,i+1}$, the stiffness elements and $c_{i,i+1}$, the damping elements; nonlinear characteristics will be addressed in Section 3 and the system matrices are not shown (they are elementary). This model can be related to a vehicle powertrain by appropriate selection of inertia and stiffness parameters. First the inertia values are selected with a comparative order of magnitude and distribution to that found in a powertrain [3]. Even though our model is generic, reference to a rear wheel drive powertrain (for the sake of illustration) could be made as follows: J_1, engine and flywheel, J_2, transmission driven gears, including clutch components, J_3, transmission output gears, any upper joint and half the propeller shaft inertia, J_4, final drive input gear (pinion), any lower joint and the other half of the propeller shaft inertia and J_5, the final drive output gears (crown wheel and differential unit). Note that for a powertrain the driven inertia is several orders of magnitude larger than the combined inertia of the torsional system, hence the grounding of the equivalent vehicle inertia for this vibration analysis. Stiffness may be related as follows: k_{12}, transmission input shaft stiffness, k_{23}, transmission mesh stiffness, k_{34}, propeller shaft stiffness, k_{45}, final drive mesh stiffness and k_5, axle and tire combined stiffness. Unity gear pairs are assumed for the sake of simplicity though there is no restriction in terms of the gear type or their radii. The next step is to specify each

mode's characteristics and then determine the stiffness parameters appropriately. We have iteratively optimized these values to give natural frequencies: $f_n = 10$, 50, 250, 1000 and 1250 Hz, with the lowest three in the order of magnitude of typical global (mode 1) and local powertrain modes. The global mode is readily excited by the transient part of $T_e(t)$ and this transient excitation (including its dependence on the mean load) is the root cause of transient impacts. In a geared system, a typical impulsive response occurs on impacts after gears pass through their clearance. The impulse excitation is at the tooth and will excite gear mesh modes that are controlled by the gear mesh stiffness associated with the Hertzian contact between teeth and the flexural stiffness of the teeth. These modes could be coupled with shaft and bearing stiffness [20]; likewise the flexural modes of thin ring structures could affect the effective mesh stiffness in case of planetary gears [21]. Further, two geared pairs may be connected by a compliant shaft element. Such is the case of a vehicle powertrain where the transmission and final drive gear sets are typically connected with single or multiple tubular propeller shafts that have many elastic deformation modes in the 1000–4000 Hz range [22]. Automotive-geared systems typically exhibit several gear mesh modes starting from 1000 Hz. Such modes may be analytically and numerically determined by using lumped formulations which have been successfully validated using experimental studies [20–21,23–25]. Since the concentration of this article is on the nonlinear torsional system, the two higher natural frequencies are selected as 1000 and 1250 Hz with dependence on k_{23}, k_{34} and k_{45} and corresponding local (mesh) modes across coordinates 2, 3 and 4.

2.3. Determination of linear system parameters and modal analysis

To determine the undamped (real) eigensolutions, Eq. (1) reduces to

$$\mathbf{J}\ddot{\boldsymbol{\theta}} + \mathbf{K}\boldsymbol{\theta} = \mathbf{0}. \tag{2}$$

Taking the generic form of a simplified vehicle system, specific natural frequencies (ω_r in rad/s for the rth mode) are defined and used to estimate the stiffness matrix, $\mathbf{K}$. The undamped system matrix, $\mathbf{A} = \mathbf{J}^{-1}\mathbf{K}$, can be defined to solve the eigenvalue problem, $\boldsymbol{\lambda}\boldsymbol{\varphi} = \mathbf{A}\boldsymbol{\varphi}$, where $\boldsymbol{\lambda}$ is the eigenvalue vector and $\boldsymbol{\varphi}$ is the modal matrix. Natural frequencies are extracted from this identity as$\omega_r = \sqrt{\lambda_r}$, $r = 1, 2, \ldots, 5$. The initial stiffness parameters are assigned values on an order of magnitude basis comparable to the powertrain. The natural frequencies are calculated using the assumed values but finalised by varying stiffness and running iterations of the eigensolutions. Note that the inertia, stiffness and damping parameters are given in Fig. 2 caption. Brief points of interest for these eigensolutions are: (a) the modes at 10 and 50 Hz are directly affected by k_{12} and k_5, which represent more compliant shafts at the engine output and the drive axles; (b) at these lower frequencies, the stiffer springs k_{23}, k_{34}, and k_{45}, create a rigid body effect across inertias J_2, J_3, and J_4; (c) k_{34} is the parameter to which the third mode (250 Hz) has the greatest sensitivity; (d) the higher frequencies, 1000 and 1250 Hz, are coupled together and are most sensitive to k_{45} and k_5; (e) the mode shapes of the five degree-of-freedom model show similar behavior to vehicle powertrains since the natural frequencies and the inertia distribution are similar.

Next, the linear system of Eq. (1) with non-proportional damping is considered. Combining $\bar{\mathbf{I}}\dot{\boldsymbol{\theta}} - \bar{\mathbf{I}}\dot{\boldsymbol{\theta}} = \mathbf{0}$, where $\bar{\mathbf{I}}$ is the identity matrix, with the linearized homogeneous form of Eq. (1) gives the expanded matrix form in terms of the state vector $\mathbf{z} = \{\dot{\boldsymbol{\theta}} \quad \boldsymbol{\theta}\}^{\mathrm{T}}$:

$$\mathbf{B}\dot{\mathbf{z}} + \mathbf{D}\mathbf{z} = \bar{\mathbf{0}}, \quad \mathbf{B} = \begin{bmatrix} \mathbf{J} & \mathbf{0} \\ \mathbf{0} & \bar{\mathbf{I}} \end{bmatrix}, \quad \mathrm{D} = \begin{bmatrix} \mathbf{C} & \mathbf{K} \\ -\bar{\mathbf{I}} & \mathbf{0} \end{bmatrix}, \quad \bar{\mathbf{0}} = \begin{Bmatrix} \mathbf{0} \\ \mathbf{0} \end{Bmatrix}. \tag{3a–d}$$

Undamped and damped natural frequencies, damping ratios and eigenvectors are obtained from the eigenvalues of $\overline{\mathbf{A}} = -\mathbf{B}^{-1}\mathbf{D}$. First the two lower modes were established with $\zeta_1 = 6\%$ and $\zeta_2 = 3\%$ by adjusting c_{12} and c_5. Then c_{34} is adjusted to obtain $\zeta_3 = 2.5\%$ and finally values $\zeta_4 = 2\%$ and $\zeta_5 = 2\%$ are attained by adjusting c_{23} and c_{45}. Other damping ratios could be used, if known say from an experiment for a given system and these ratios have been assigned as 'ball park' and linearised values.

3. Nonlinear transient analysis

3.1. Torque excitations and clearance algorithm

For nonlinear transient analysis the excitation, $T_e(t)$, includes a initial part, T_m and a ramp function commencing at $t = t_a$, with magnitude, ΔT_m, and of duration $\tau = t_b - t_a$:

$$T_e(t) = \begin{cases} T_m, & t \leqslant t_a, \\ T_m + \Delta T_m (t - t_a)/\tau, & t_a < t < t_b, \\ T_m + \Delta T_m, & t \geqslant t_b. \end{cases} \tag{4}$$

Clearance is modelled using the piecewise characteristics described below and shown in Fig. 1b. Here, $\delta_{i,i+1}$, represents the clearance for the $(i,i+1)$th stiffness element and $\psi_{i,i+1} = \theta_i - \theta_{i+1}$,

$$k_{i,i+1} = \begin{cases} k_{i,i+1}, & |\psi_{i,i+1}| \geqslant 0.5\delta_{i,i+1}, \\ 0, & |\psi_{i,i+1}| < 0.5\delta_{i,i+1}. \end{cases} \tag{5}$$

With the gear mesh torque, $T_{i,i+1}$, modelled as such, the torque vector of Eq. (1) needs to account for the offset of torque from the zero position [26] (Fig. 1b shows the offset from the linearised stiffness). Hence, torque offsets are included in the vector as

$$T_{\delta(i)} = 0.5 \operatorname{sign}(\psi_{i,i+1}) k_{i,i+1} \delta_{i,i+1}, \quad T_{\delta(i+1)} = -0.5 \operatorname{sign}(\psi_{i,i+1}) k_{i,i+1} \delta_{i,i+1}. \tag{6a, b}$$

When the stiffness, $k_{i,i+1}$, is found to be zero, these torque offset are returned as zero. In the following evaluations of the proposed metrics, the clearance has been assigned only to the location k_{23} with magnitude $\delta_{23} = 0.001$ rad. Thus the global torque vector of Eq. (1) includes the transient excitation, Eq. (4) and torque offsets, Eq. (6a, b) for $i = 2$:

$$\mathbf{T}(\theta, t) = \begin{bmatrix} T_e(t) & T_{\delta 2}(\theta) & T_{\delta 3}(\theta) & 0 & 0 \end{bmatrix}^{\mathrm{T}}, \tag{7}$$

To understand the impulsive responses, we define a map of torque excitations, denoted by the following matrix, $\bar{\mathbf{M}}$, where a column vector, $\mathbf{T}_m$, includes j initial torques, $(T_m)_j$, and is used to form the matrix of j row vectors, $(\Delta \mathbf{T}_m)_j$, where the kth element of each row is a magnitude, $(\Delta T_m)_{j,k}$, for the ramp, where $j = 1,2,\ldots,5$ and $k = 1,2,\ldots,9$:

$$\bar{\mathbf{M}} = [\Delta \mathbf{T}_m], \quad \mathbf{T}_m = \begin{bmatrix} 40 & 60 & 80 & 100 & 120 \end{bmatrix}^{\mathrm{T}}, \tag{8a, b}$$

$$(\Delta T_m)_j = -\left[\frac{(T_m)_j}{1.4} \quad \frac{(T_m)_j}{1.3} \quad \frac{(T_m)_j}{1.2} \quad \frac{(T_m)_j}{1.1} \quad (T_m)_j \quad 1.1(T_m)_j \quad 1.2(T_m)_j \quad 1.3(T_m)_j \quad 1.4(T_m)_j \right]. \tag{8c}$$

Also in the following simulations, $t_a = 0.025$ s, $t_b = 0.075$ s and $\tau = 0.05$ s. The map provides a set of 45 solutions.

3.2. Initial conditions

The initial angular velocity vector is simply $\dot{\boldsymbol{\theta}}(0) = 0$. An initial angular displacement vector, $\bar{\boldsymbol{\theta}}(0)$, is first determined using the linearised stiffness at clearance locations. With an initial torque vector, $\bar{\mathbf{T}}(0) = [\, T_e(t) \quad 0 \quad 0 \quad 0 \quad 0 \,]^{\mathrm{T}}$ it is defined as

$$\bar{\boldsymbol{\theta}}(0) = \mathbf{K}^{-1} \bar{\mathbf{T}}(0). \tag{9}$$

Then angular displacement offsets are applied to account for the torque offsets shown for the ith coordinates as Eq. (6a, b) and that are applied within the torque vector, Eq. (7). In this case, with a single clearance, the coordinates upstream of element, $i = 2$ are rotated through half the clearance δ_{23}, with direction depending on the value of initial torque, $(T_m)_j$:

$$\theta_1(0) = \bar{\theta}_1(0) + 0.5 \operatorname{sign}(T_m)_j \delta_{23}, \quad \theta_2(0) = \bar{\theta}_2(0) + 0.5 \operatorname{sign}(T_m)_j \delta_{23}. \tag{10a,b}$$

This yields the initial angular displacement vector, $\boldsymbol{\theta}(0) = [\, \theta_1(0) \quad \theta_2(0) \quad \bar{\theta}_3(0) \quad \bar{\theta}_4(0) \quad \bar{\theta}_5(0) \,]^{\mathrm{T}}$.

3.3. Sample simulation

The system of governing equations, Eq. (1), is nonlinear and the solutions are programmed in Matlab with 'ODE15S', a solver that uses Gear's Method for stiff systems [27]. A sample simulation is used to illustrate the nature of solutions, define the main events of interest and to suggest qualitative metrics. This simulation is for

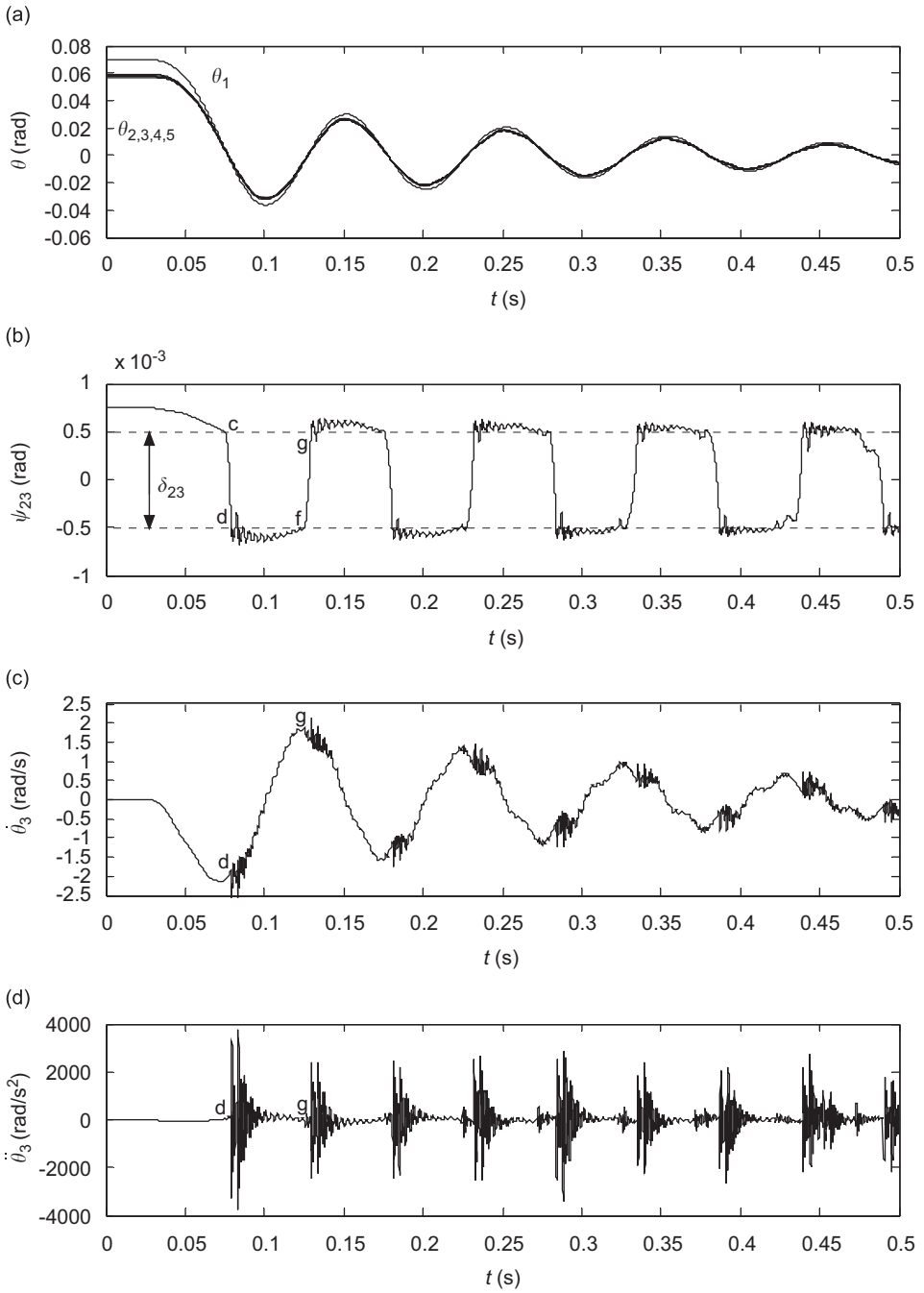

Fig. 3. Sample results for impulse response with excitation parameters $T_m = 80\,\text{Nm}$, $\Delta T_m = -T_m$, $t_a = 0.025\,\text{s}$, $t_b = 0.075\,\text{s}$, $\tau = 0.05\,\text{s}$. (a) Angular displacements for all coordinates, (b) relative angular displacement, $\psi_{23} = \theta_2 - \theta_3$, across nonlinear stiffness element, k_{23}, (c) angular velocity, $\dot{\theta}_3$, (d) angular acceleration, $\ddot{\theta}_3$.

the midpoint of the torque excitation map, $\overline{M}_{3,5}$. Fig. 3a provides time histories for coordinate angular displacements. For the sake of clarity, events of interest are referred to as t_p with index, $p = a,b,\ldots,h$. Note that the system is stationary with initial twist, $\boldsymbol{\theta}(0)$, balancing the initial torque until the ramp-down commences at $t_a = 0.025$ s. Points a and b refer to the beginning and end of the torque ramp-down (not shown in figures). Then transient response for displacements stays within a small envelope of the linear solution that could be defined by setting $\delta_{23} = 0$. Evident in this plot is response at the lowest mode at 10 Hz. Also, notice the reversal in torque during each cycle (crossing from positive to negative displacement). Fig. 3b shows the relative angular displacement, $\psi_{23} = \theta_2 - \theta_3$, with first pass into clearance at point c and impacts when exiting clearance at point d; similarly for points f and g. Points d and g are defined as the primary impacts. Thus

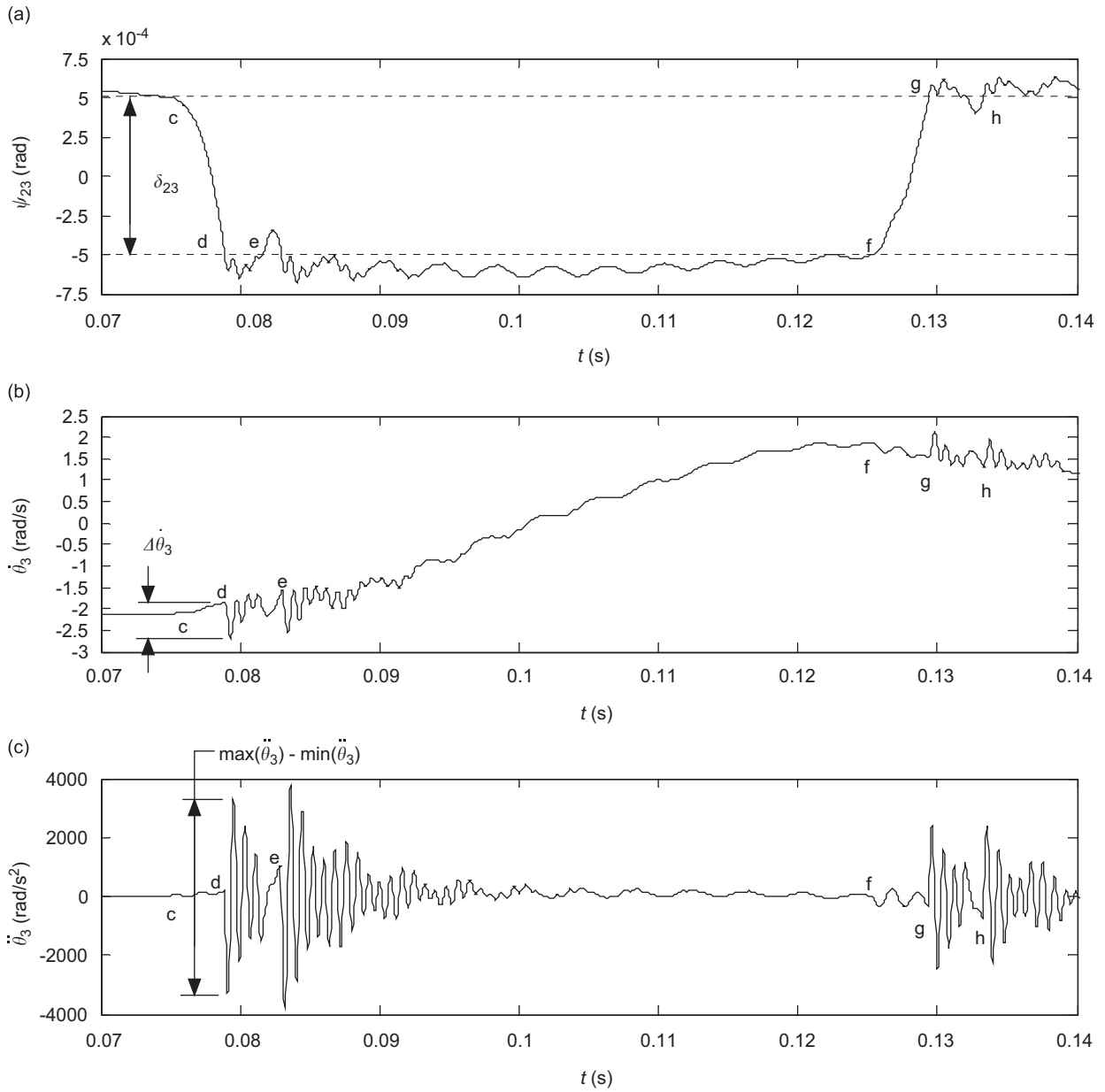

Fig. 4. Sample results for impulse response for $\{0.07 < t < 0.14\}$ with excitation parameters $T_m = 80$ N m, $\Delta T_m = -T_m$, $t_a = 0.025$ s, $t_b = 0.075$ s, $\tau = 0.05$ s: (a) relative angular displacement, $\psi_{23} = \theta_2 - \theta_3$, across nonlinear stiffness element, k_{23}; (b) angular velocity, $\dot{\theta}_3$, with illustration of metric $Q_4 = \Delta\theta_3$; (c) angular acceleration, $\ddot{\theta}_3$, with illustration of metric $Q_6 = \max(\ddot{\theta}_3) - \min(\ddot{\theta}_3)$.

separation has occurred in the domains $\{t_c < t < t_d\}$ and $\{t_f < t < t_g\}$. Note that points a and b are defined by the torque excitation. With a single nonlinearity in the system at k_{23}, the most significant impulse response occurs at θ_3, where the lightest inertia is coupled directly to the nonlinear stiffness. Fig. 3c shows the angular velocity of this inertia, where the impulse responses, in this case two or more times per cycle of the lowest mode, are clearly evident. Fig. 3d shows corresponding angular accelerations. This result resembles gear rattle (or periodic vibro-impact) characteristics, this is as $T_e(t) = 0$ for $t \geqslant t_b$; other points in $\overline{\mathbf{M}}$ have less impacts. Also this repetitive impulsive behavior dies out soon after $t \geqslant 0.5$ s. Fig. 4a–c provides the solution results over $\{0.07 < t < 0.14\}$, where two more events of interest are defined, points e and h, as secondary impacts. Here the contacting bodies have rebounded and impacted again without passing significantly back into clearance. Observe that these impacts do not occur while following the motions of the lowest mode of vibration, rather on rebound from a primary impact.

3.4. Convergence study

Convergence is studied to ensure the time resolution and tolerance yield an accurate solution. The Matlab solver [27] employs a variable time step (Δt) algorithm which reduces Δt to meet relative and absolute tolerances of error; it also has an option to limit the maximum time resolution, $\Delta t_{\max}$, which when small $\Delta t_{\max}$ forces the solver to take smaller steps before reaching the discontinuity, we have found this effective for these clearance problems. We have assigned, $\Delta t_{\max} = 4 \times 10^{-5}$, a relative tolerance of $\varepsilon_r = 1 \times 10^{-3}$ and absolute tolerance of $\varepsilon_a = \varepsilon_r/1000$; two convergence studies establish these parameters: Study I holds $\Delta t_{\max}$ constant and varies ε_r and Study II holds ε_r constant and varies $\Delta t_{\max}$. Solutions are found for the extreme point of $\overline{\mathbf{M}}$, where $(T_m)_5 = 120\,\mathrm{N\,m}$ and $(\Delta T_m)_{5,9} = -1.4(T_m)_5$. Figs. 5a and b provide the global time histories for ψ_{23} and $\ddot{\theta}_3$ with the default values, $\Delta t_{\max} = 4 \times 10^{-5}$ s, $\varepsilon_r = 1 \times 10^{-3}$ and $\varepsilon_a = 1 \times 10^{-6}$. Note the differences here with $\bar{M}_{5,9}$ to solutions shown in Fig. 3, for $\overline{M}_{3,5}$. In this case there is a large negative torque after the ramp-down, hence the system stays twisted to one side. Convergence is assessed for $\underline{\ddot{\theta}}_s = \ddot{\theta}_3(t)$ *at* $t \approx t_d$, which is taken as the minimum peak of $\ddot{\theta}_3$ following the first primary impact (point d), highlighted in Fig. 5b as the region of interest, where s designates the case index. For each of the Figs. 5c and 5d the results are shown within this region for Study I and Study II; Tables 1 and 2 provide corresponding values for $\underline{\ddot{\theta}}_s$. The quantifying parameter is defined as $\Gamma_s = 100(\underline{\ddot{\theta}}_s/\underline{\ddot{\theta}}_n)$ for $s = 1, 2, \ldots, n$; the percentage variation from the case with the finest, $\varepsilon_r = 6.25 \times 10^{-5}$, $s = n = 5$ (Study I), or smallest $\Delta t_{\max} = 1.25 \times 10^{-6}$ s, $s = n = 5$ (Study II). Assessing Study I it can be seen that there is little difference in Γ for all values of ε_r. Given $\Gamma \leqslant \pm 0.05\%$ for $\varepsilon_r \leqslant 5 \times 10^{-4}$, we have selected this as the upper bound for ε_r. Study II shows the greater sensitivity to the maximum time stepping. Also, that convergence does not follow the trend typical for a linear system. The variable stepping algorithm in combination with $\Delta t_{\max}$ causes the solver to 'step over' the discontinuity in a different manner for each case, with a successful step once tolerances are satisfied. Case $s = 1$ with the lowest value, $\Gamma_1 = -0.08$, illustrates this non-monotonic convergence. Given that $\Gamma < \pm 0.9\%$ for $\Delta t_{\max} \leqslant 4 \times 10^{-5}$ s we have selected this as the upper bound for $\Delta t_{\max}$. This choice of solver parameters should yield good results for the purpose of evaluating metrics and yet provide a balance of computational efficiency versus accuracy, given that $\overline{\mathbf{M}}$ requires 45 solutions and associated post-processing.

4. Development of metrics to quantify the impulsive source

Metrics to quantify the response(s) from impact(s) are classified into three groups: (1) global metrics that provide information over the entire time domain; (2) metrics determined immediately prior to impact; (3) metrics determined following an impact. The metrics are symbolically denoted as Q_q for $q = 1,2,\ldots,7$.

4.1. Global metric

Metric 1, Q_1, considers the entire time history of the signal. Each time the relative displacement passes through clearance on both sides of the origin, the event is considered a double-sided impact. In Fig. 3b, this event would include solution flow through points d and g. A single-sided impact describes a system response is the case where the solution flow passes through point d only. Secondary impacts may or may not occur in

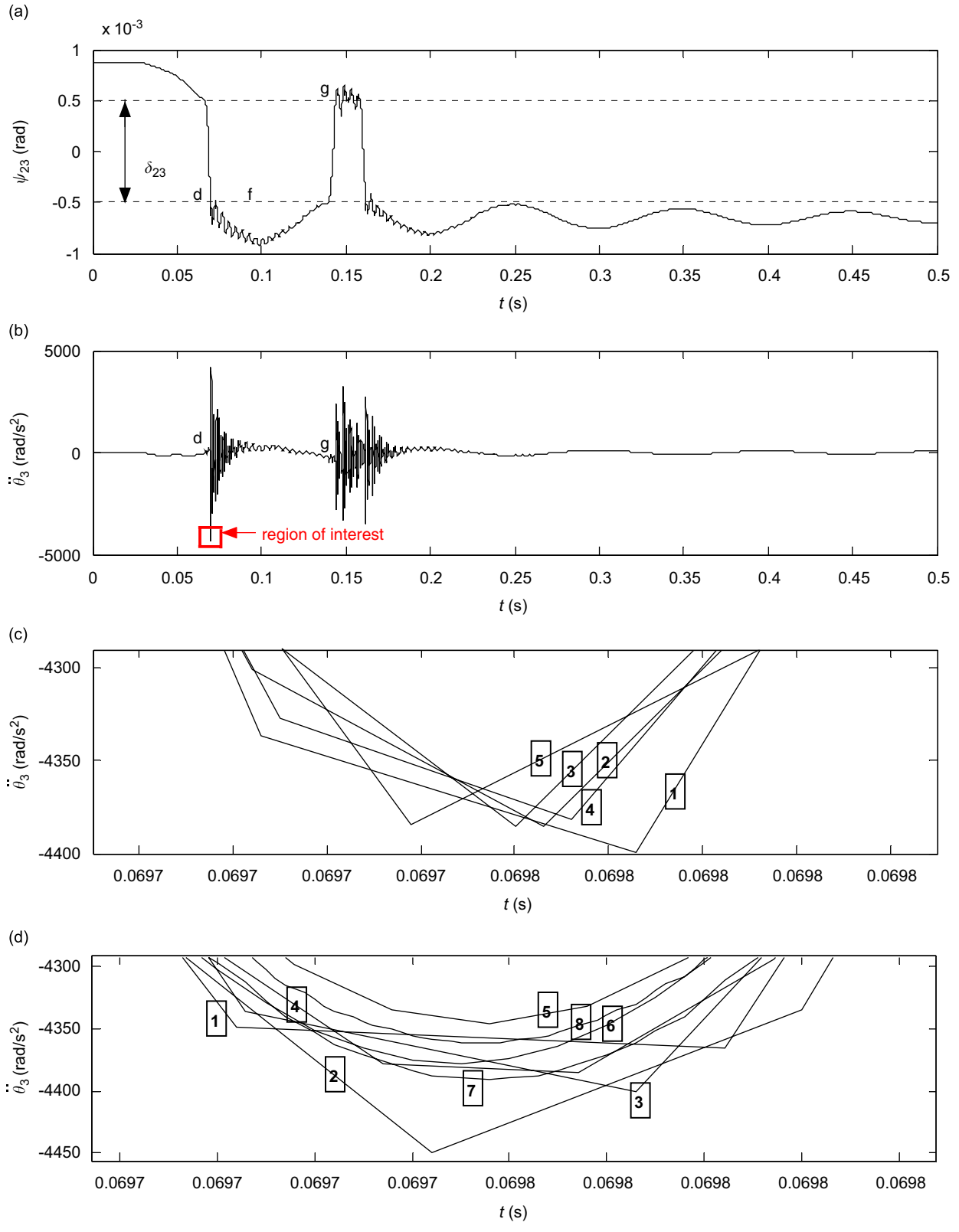

Fig. 5. Results for numerical convergence study with excitation parameters $T_m = 120$ Nm, $\Delta T_m = -T_m/1.4$, $t_a = 0.025$ s, $t_b = 0.075$ s, $\tau = 0.05$ s: (a) relative angular displacement, $\psi_{23} = \theta_2 - \theta_3$, across nonlinear stiffness element, k_{23}, and (b) angular acceleration, $\ddot{\theta}_3$, both with $\Delta t_{\max} = 4 \times 10^{-5}$ s and $\varepsilon_r = 1 \times 10^{-3}$; (c) Study I results: angular acceleration, $\ddot{\theta}_3$, for $\{0.069715 < t < 0.069805\}$ with $\Delta t_{\max} = 4 \times 10^{-5}$ s and ε_r varied as per Table 1; (d) Study II results: angular acceleration, $\ddot{\theta}_3$, for $\{0.69715 < t < 0.069805\}$ with $\varepsilon_r = 1 \times 10^{-3}$ and $\Delta t_{\max}$ varied as per Table 2.

Table 1
Convergence study I: $\underline{\ddot{\theta}}_s$ and Γ_s values for variation in tolerances, ε_r and $\varepsilon_a = \varepsilon_r/1000$

Case, s	ε_r	$\underline{\ddot{\theta}}_s$ (rad/s^2)	Γ_s (%)
1	1.00E−03	−4400	−0.36
2	5.00E−04	−4385	−0.02
3	2.50E−04	−4385	−0.02
4	1.25E−04	−4382	0.05
5	6.25E−05	−4384	0.00

Table 2
Convergence study II: $\underline{\ddot{\theta}}_s$ and Γ_s values for variation in maximum time resolution, $\Delta t_{\max}$

Case, s	$\Delta t_{\max}$ (s)	$\underline{\ddot{\theta}}_s$ (rad/s^2)	Γ_s (%)
1	1.60E−04	−4365	−0.09
2	8.00E−05	−4450	−2.04
3	4.00E−05	−4400	−0.89
4	2.00E−05	−4386	−0.57
5	1.00E−05	−4346	0.34
6	5.00E−06	−4378	−0.39
7	2.50E−06	−4391	−0.69
8	1.25E−06	−4361	0.00

Table 3
Definitions for metric 1, Q_1, number and nature of impacts

Q_1	Definitions for Q_1 metric
0	No impacts
$S(1)$	One single-sided primary impact
$S(m)$	Multiple single-sided primary impacts
$D(1)$	One double-sided primary impact
$D(m)$	Multiple double-sided primary impacts

either case. The number of impact events is defined as no impact, a single impact, or multiple impacts. Table 3 provides the classification for Q_1. The solutions shown in Fig. 3b would be classified as $D(m)$-multiple double-sided impact events as would those in Fig. 5a; here for sake of simplicity the double sided impact followed by a single side impact is classified as $D(m)$.

4.2. Metric determined prior to impact

Relative Kinetic Energy: Just prior to impact, e.g. $t = t_d - \Delta t$, the colliding bodies have a certain difference in kinetic energy, which is examined for viability as a metric; here the sign of velocity is included so as to measure 'relative' kinetic energy,

$$Q_2 = \left| 0.5 J_2 \dot{\theta}_2^2 \mathrm{sign}(\dot{\theta}_2) - 0.5 J_3 \dot{\theta}_3^2 \mathrm{sign}(\dot{\theta}_3) \right| \tag{11}$$

Relative angular acceleration: With similar consideration as the above metric, the relative angular acceleration metric is determined just prior to impact as

$$Q_3 = \ddot{\theta}_2 - \ddot{\theta}_3. \tag{12}$$

The accelerations may be extracted during numerical solutions, otherwise they can be evaluated at the post-processing stage from $\ddot{\theta}_2 = [k_{12}(\theta_1 - \theta_2) + c_{12}(\dot{\theta}_1 - \dot{\theta}_2)]/J_2$ and $\ddot{\theta}_3 = [-k_{34}(\theta_3 - \theta_4) - c_{34}(\dot{\theta}_3 - \dot{\theta}_4)]/J_3$.

4.3. Metrics determined following impact

Instantaneous change in angular velocity: The instantaneous change in angular velocity relates to a change in momentum after impact. To examine the effect of inertia we select J_3 since $J_3 \ll J_2$. Prior to impact, $\dot{\theta}_3$ follows the motion at the lowest mode. At impact $\dot{\theta}_3$ suddenly changes and then includes a decaying response at higher frequency modes. The instantaneous change in angular velocity measured from the impact point to the first peak should quantify this impulse (shown in Fig. 4b):

$$Q_4 = \Delta\dot{\theta}_3. \tag{13}$$

Instantaneous change in interfacial torque: The interfacial torque across the clearance element is expanded from Eq. (1) as the expression for the combined torques of k_{23} and c_{23}, including the conditions governed by the clearance algorithm, Eq. (5):

$$T_{23} = k_{23}(\theta_2 - \theta_3) - T_{\delta 3} + c_{23}(\dot{\theta}_2 - \dot{\theta}_3). \tag{14}$$

Fig. 6a provides T_{23} for the sample simulation of Section 3.3. The metric is taken from the impact point to the first peak (Fig. 6b):

$$Q_5 = \Delta T_{23}. \tag{15}$$

Peak to peak angular acceleration: Similar to Q_4 and Q_5, peak to peak acceleration is a response due to the initial impulse. Again considering J_3 as the body of interest and the maximum and minimum as the first peaks to occur after the impact (Fig. 4c):

$$Q_6 = \max(\ddot{\theta}_3) - \min(\ddot{\theta}_3). \tag{16}$$

Time windowed mean-square angular acceleration: Examining Fig. 4c it can be seen that following the impact at point d there is a ringing effect and within a short time span comes the secondary impact. It is desirable to determine the mean square quantity so as to account for mainly the first impact and reduce the significance of

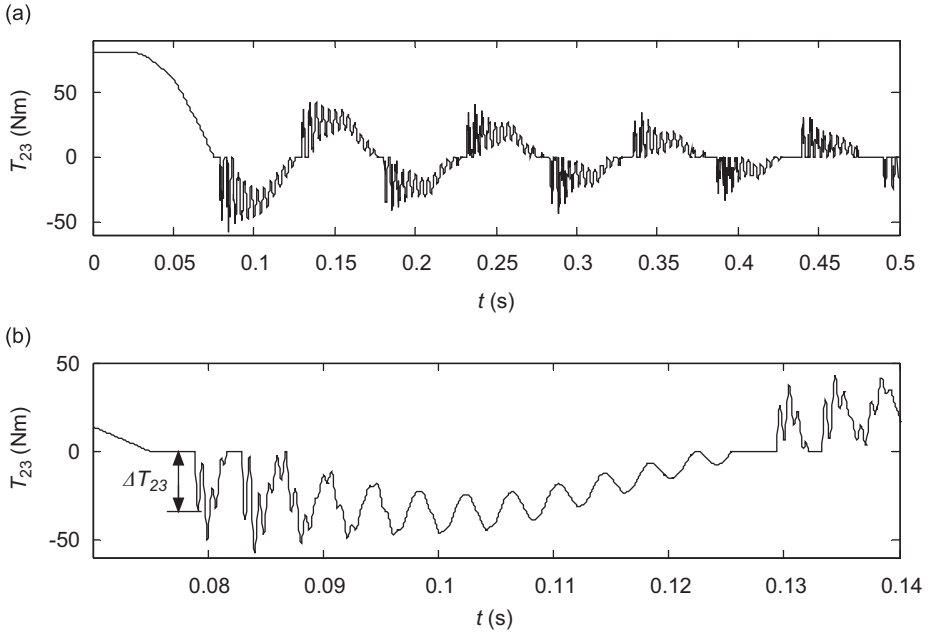

Fig. 6. Interfacial torque, T_{23}, for simulation with excitation parameters $T_m = 80\,\text{Nm}$, $\Delta T_m = -T_m$, $t_a = 0.025\,\text{s}$, $t_b = 0.075\,\text{s}$, $\tau = 0.05\,\text{s}$: (a) entire solution domain; (b) for domain $\{0.07 < t < 0.14\}$ with illustration of metric $Q_5 = \Delta T_{23}$.

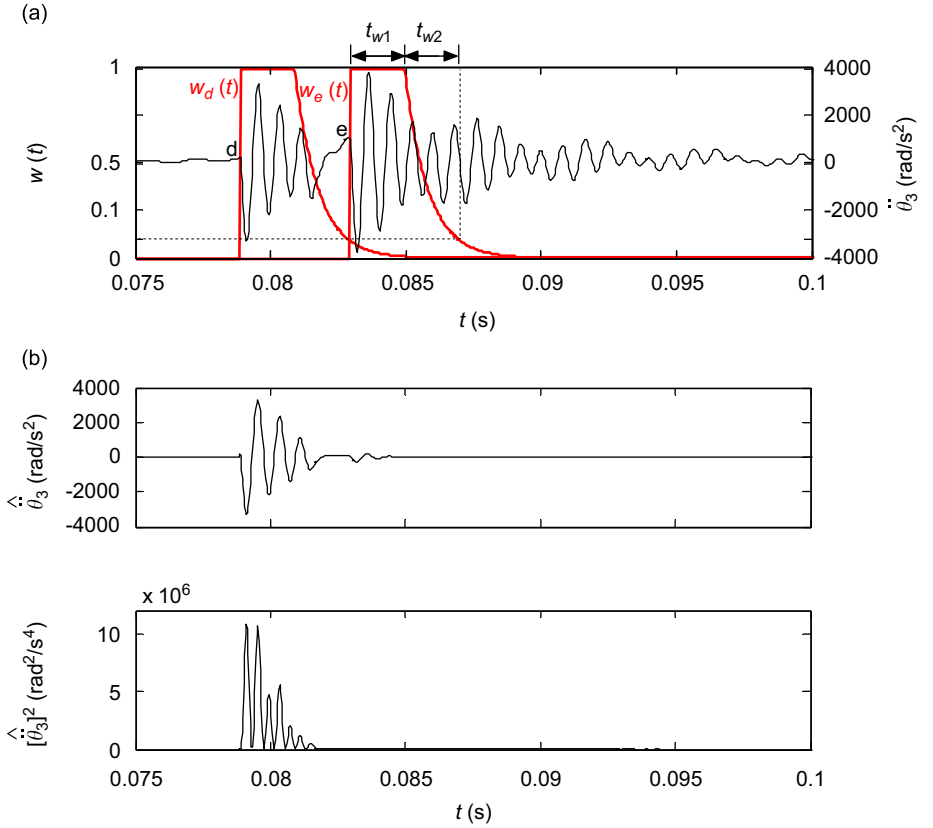

Fig. 7. Illustration for determination of metric Q_7, mean-square acceleration: (a) angular acceleration, $\ddot{\theta}_3$, and windowing function as applied for Point *d* and *e*; (b) time-windowed angular acceleration, $\hat{\ddot{\theta}}_3$ and squared time-windowed angular acceleration $\hat{\ddot{\theta}}_3^2$, for Point *d*.

this ringing. This metric can be designed to include the responses of closely spaced multiple impacts and assist with experimental measurements. The following window is proposed via a combination of a step and an exponentially decaying function:

$$w(t) = \begin{cases} 0, & t < t_p, \\ 1, & t_p \leqslant t < t_p + t_{w1}, \\ e^{\xi[t-(t_p+t_{w1})]}, & t \geqslant t_p + t_{w1}. \end{cases} \tag{17}$$

Here t_p only includes indexes defined as a point of impact, i.e. $t_p = t_d$ when considering point *d*; likewise $t_p = t_e$ when considering point *e*. Fig. 7a overlays $w(t)$ with $\ddot{\theta}_3$, for both impacts. The step window has duration, $t_{w1} = 0.002$ s, in this instance, allowing time to capture response of two complete cycles at 1000 Hz or 2.5 cycles at 1250 Hz, which are the two highest natural frequencies of the linearised system. The decaying window function is defined so that $e^{\xi[t-(t_p+t_{w1})]} = 1$ at its commencement, i.e. $t = t_p + t_{w1}$ Also, it is defined so that after a specified time, $t_{w2} = 0.002$ s, the window provides a weighting of 10% of the original signal, i.e. $e^{\xi[t-(t_p+t_{w1})]} = 0.1$, at $t = t_p + t_{w1} + t_{w2}$. After this time any data can be effectively considered to be 'wiped away'. Given these two points in the decay function the decay parameter is determined as $\xi = \ln(0.1/t_{w2})$. To obtain the metric, the acceleration signal is first windowed, $\hat{\ddot{\theta}}_3(t) = \ddot{\theta}_3(t)w(t)$ and then the mean-square windowed angular acceleration is computationally determined as

$$Q_7 = \frac{1}{t_{w1} + t_{w2}} \int_{t_k}^{t_k+t_{w1}+t_{w2}} \hat{\ddot{\theta}}_3^2 \, dt. \tag{18}$$

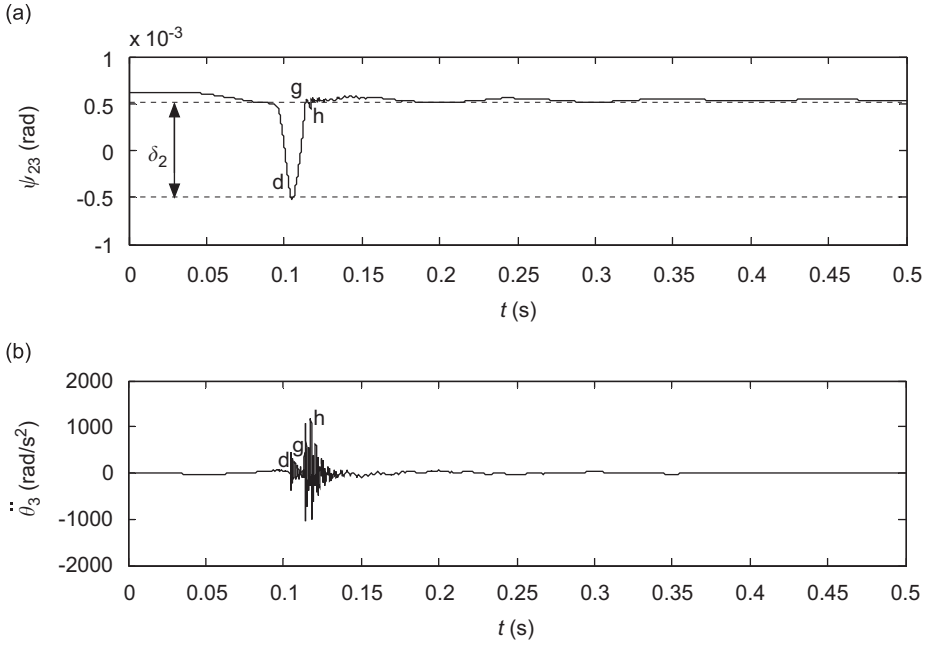

Fig. 8. Sample results for impulse response with excitation parameters $T_m = 40\,\text{Nm}$, $\Delta T_m = -T_m/1.4$, $t_a = 0.025\,\text{s}$, $t_b = 0.075\,\text{s}$, $\tau = 0.05\,\text{s}$. (a) Relative angular displacement, $\psi_{23} = \theta_2 - \theta_3$, across nonlinear stiffness element, k_{23}; (b) angular acceleration, $\ddot{\theta}_3$.

For this metric, the parameters t_{w1} and t_{w2} should be carefully selected depending on the modal properties of the system and the nature of nonlinear solutions. Fig. 7b provides $\hat{\ddot{\theta}}_3(t)$ and $\hat{\ddot{\theta}}_3^2(t)$ for point d.

5. Comparative evaluation and application of metrics

5.1. Comparison of metrics over a map of transient excitations

Each of the above metrics have been calculated as $(\mathbf{Q}_q)_p$, over the excitation map, $\bar{\mathbf{M}}$. Recall that one clearance was specified at location k_{23}. The result for the global metric, in terms of the *number and nature of impacts*, is $D(1)$ with $\bar{\mathbf{M}}_{j,1}$ for all j and $D(m)$ for all other points $\bar{\mathbf{M}}$; most of the solutions within the map feature multiple double sided impacts. Two examples of this type have already been illustrated: Fig. 3 for the center of $\bar{\mathbf{M}}$ ($j = 3$, $k = 5$) and Fig. 5 for the lower far right corner ($j = 5$, $k = 9$). For the sake of comparison, Figs. 8a and b provide the results for the top right corner of $\bar{\mathbf{M}}$ ($j = 1$, $k = 1$), where there is only one double-sided impact. In this case the transient excitation from the torque ramp was just sufficient to cause a torque reversal between the meshing elements. There is a small impact after crossing the origin of relative displacement at point d and then a larger impact at point g after crossing back over the origin and a secondary impact of similar magnitude at point h. After the ramp-down, $T_e(t) = T_m - (T_m/1.4) > 0$, thus the system remains in condition of positive twist which is eventually static after the transients decay. Whereas for the simulation of Fig. 5, after the final impact, $T_e(t) = T_m - 1.4T_m < 0 T_e(t) = T_m - 1.4T_m < 0$, so the system response decays to leave a negative static twist.

The metrics just prior to and following impact have been calculated for impacts at points $p = d,e,g$ and h. Here, we show comparisons for points d and e and briefly discuss points g and h. Surface $(\mathbf{S}_q)_p$ and line $(\mathbf{L}_q)_{p,j}$ mappings (Figs. 9 and 10) have been constructed versus $(\Delta\mathbf{T}_m)_j$, $\mathbf{T}_m$, and $(\mathbf{Q}_q)_p$ where $(\Delta\mathbf{T}_m)_j \Big/ (T_m)_j = -\begin{bmatrix} 1/1.4 & 1/1.3 & 1/1.2 & 1/1.1 & 1 & 1.1 & 1.2 & 1.3 & 1.4 \end{bmatrix}$, $j = 1,2,\ldots,$or 5. Here $(\mathbf{Q}_q)_p$ is a set of metrics where q is the metric index (2 to 7). Further, each metric may be normalized to the maximum value in $(\mathbf{Q}_q)_p$ or in the case where a negative minimum has the greatest magnitude. Note, a single value in $(\mathbf{Q}_q)_p$ is $(Q_q)_{p,j,k}$.

The line plots, $(\mathbf{L}_q)_{p,j}$, allow a thorough evaluation of the effectiveness of each metric by comparing normalized values, on the other hand, the surface maps, $(\mathbf{S}_q)_p$, provide a better understanding of the effect of initial torque versus ramp-down on the impulsive responses at different points, p.

From the figures there is an obvious correlation between the metrics quantified for response following impact, Q_4 through to Q_7. The metrics quantified for relative kinetic energy, Q_2, and relative acceleration,

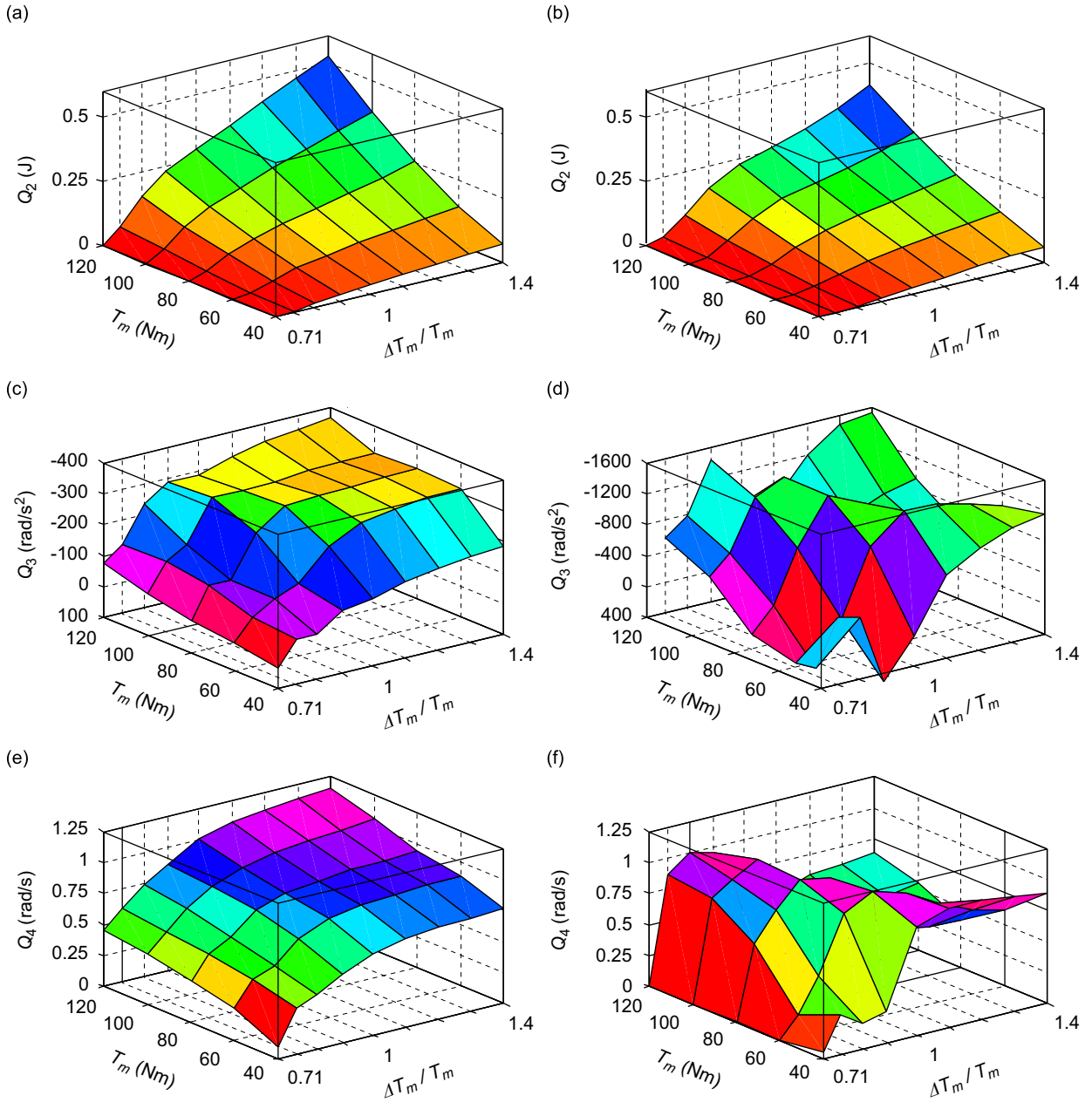

Fig. 9. Surface maps of metrics over transient excitation map: (a)–(b) Q_2 vs. $\tilde{\mathbf{M}}$: relative kinetic energy just prior to impact; (c)–(d) Q_3 vs. $\tilde{\mathbf{M}}$: relative acceleration just prior to impact; (e)–(f) Q_4 vs. $\tilde{\mathbf{M}}$: instantaneous change in velocity just after impact; (g)–(h) Q_5 vs. $\tilde{\mathbf{M}}$: instantaneous change in interfacial torque just after impact; (i)–(j) Q_6 vs. $\tilde{\mathbf{M}}$: peak to peak acceleration just after impact; (k)–(l) Q_7 vs. $\tilde{\mathbf{M}}$: time windowed mean-square acceleration just after impact. Subfigures (a), (c), (e), (g), (i) and (k) are for the primary impact at Point d, and (b),(d),(f),(h),(j) and (l) for the secondary impact at Point e.

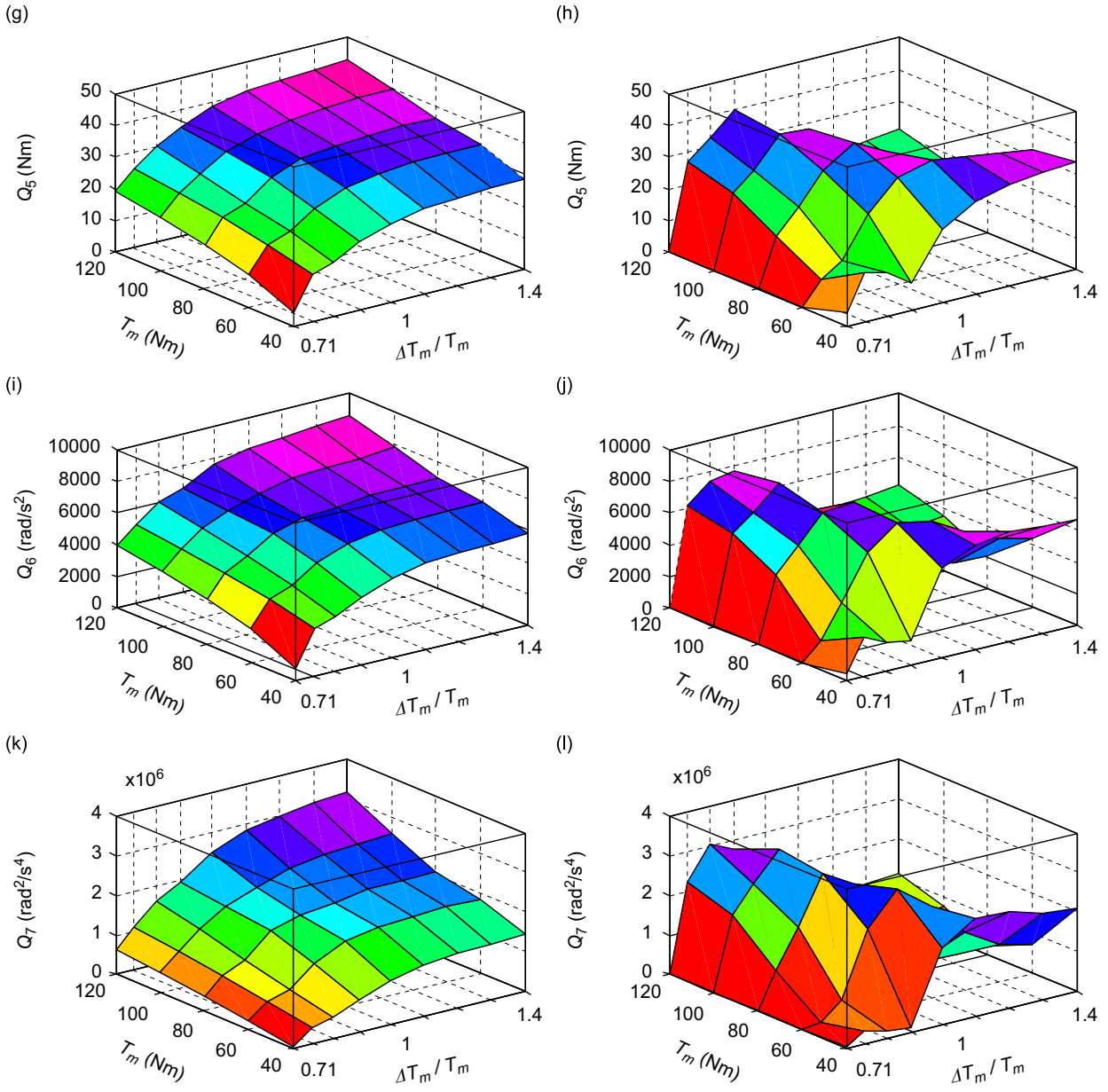

Fig. 9. (*Continued*)

Q_3, just prior to impact do not follow the trend, with exception of Q_3 for point d. This will be discussed in Section 6. Fig. 10 provides the line plots, $(L_q)_{p,j}$, for each element $(T_m)_j$. Examining the primary impact at point d it can be seen that the metrics for instantaneous change in angular velocity, instantaneous change in interfacial torque and peak to peak angular acceleration, Q_4, Q_5 and Q_6, provide practically the same results. For the secondary impact at point e they correlate closely, yet not as well as for point d. The metric for time windowed mean-square acceleration, Q_7, follows the same trend as the others but has significant difference. Rather than just using visual inspection, a method of quantifying the difference is proposed as: Compute and compare the mean sum of the ratioed difference between normalized metrics. For example, taking, $(\underline{\hat{Q}}_{4/3})_p = \frac{1}{45}\sum_{j=1,k=1}^{j=5,k=9}[(\hat{Q}_4)_{p,j,k}/(\hat{Q}_3)_{p,j,k}]$, gives the mean sum of each point in $(\hat{\mathbf{Q}}_4)_p$ divided by corresponding

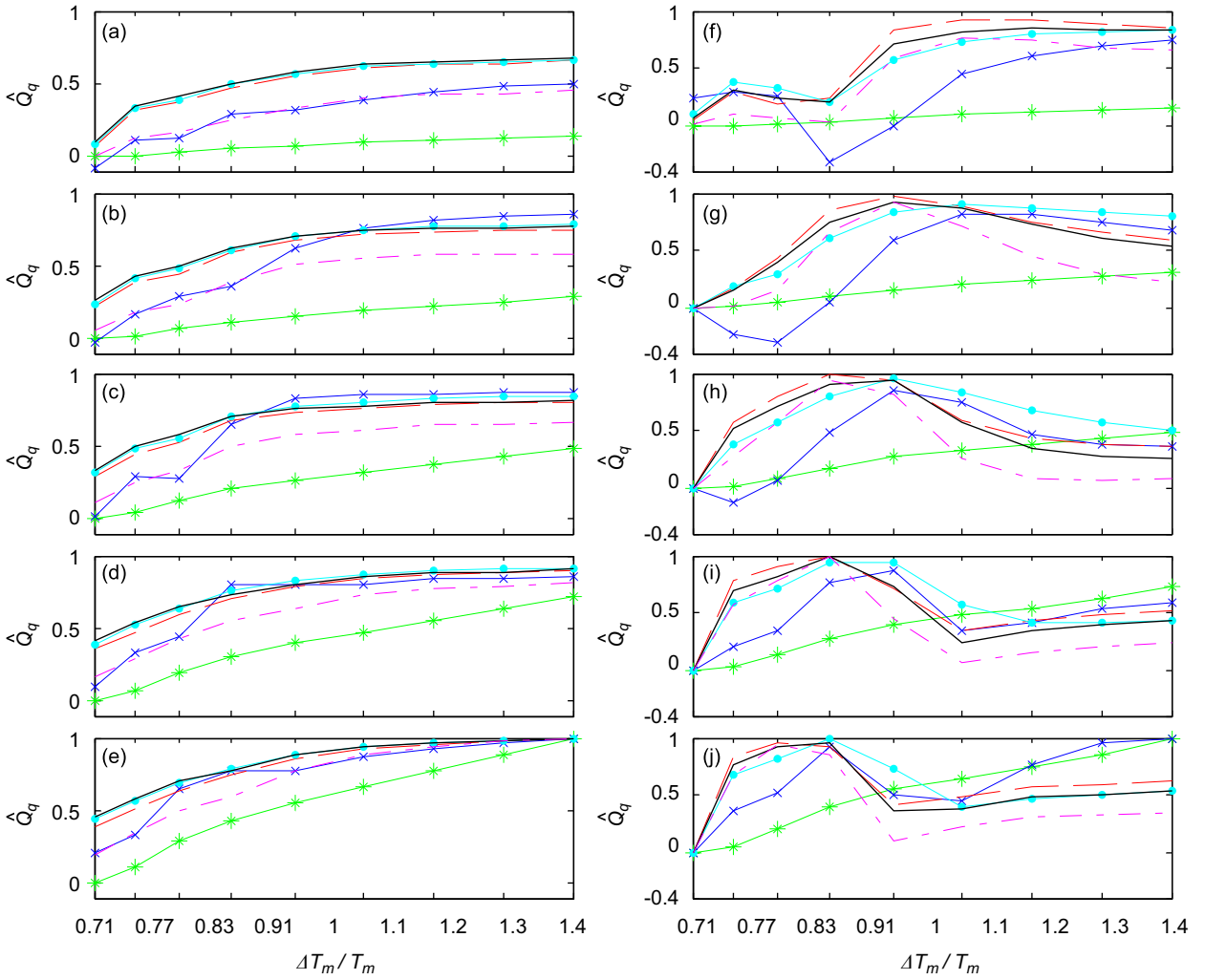

Fig. 10. Line plots showing normalized metrics vs. $\Delta\mathbf{T}_m/\mathbf{T}_m$ for each point in $\mathbf{T}_m = \begin{bmatrix} 40 & 60 & 80 & 100 & 120 \end{bmatrix}^{\mathrm{T}}$: (a)–(e) primary impact at point d; (f)–(j) secondary impact at point e, with (a) $T_m = 40$, (b) $T_m = 60$, (c) $T_m = 80$, etc. Key: Q_2 Q_3 Q_4 Q_5 Q_6 Q_7.

points in $(\hat{\mathbf{Q}}_3)_p$ (note, reciprocal values, e.g. $(\hat{\underline{Q}}_{3/4})_p$, are not calculated). Considering only the four metrics for after impact, $(\hat{Q}_{r/q})_p$, yields six distinct mean deviations, as shown in Tables 4a–d for points d, e, g and h respectively. This more clearly quantifies the above statements on differences between each metric, i.e.; for $p = d$ and g, $(\hat{Q}_{r/q} - 1)_p$ lies within ± 0.06 ($r = q = 4{,}5{,}6$), and $(\hat{Q}_{7/q} - 1)_p$ within ± 0.43 ($q = 4{,}5{,}6{,}7$); for $p = e$ and h $(\hat{Q}_{r/q} - 1)_p$ lies within ± 0.17 and $(\hat{Q}_{7/q} - 1)_p$ within ± 0.49. The large difference in Q_7 is as it is an energy quantity, by taking $(Q_7^*)_{p,j,k} = \sqrt{(Q_7)}_{p,j,k}$ it can be directly related to Q_4, Q_5 and Q_6. The tables show that the mean deviation, $(\hat{Q}^*_{7/q})_p$, is now on a similar order to $(\hat{Q}_{r/q})_p$. In line plots, $(\mathbf{L}_q)_{j,p}$, the new quantity $\hat{\mathbf{Q}}^*_7$ tracks the metrics measured after impact closely (plot not shown). For kinetic energy, taking, $(Q_2^*)_{p,j,k} = \sqrt{(Q_2)}_{p,j,k}$, similarly relates the measurement to torque, velocity or acceleration, however this does not improve the correlations. In the context of signal processing, Q_2 and Q_7 are volt^2-second quantities, and Q_3, Q_4, Q_5 and Q_6 are volt-second quantities.

Table 4
Mean deviations between normalised metrics measured after impact: (a) Point d; (b) Point e; (c) Point g; (d) Point *h*

(a)	1			
$\hat{Q}_4$				
$\hat{Q}_5$	1.05	1		
$\hat{Q}_6$	1.06	1.01	1	
$\hat{Q}_7$	0.70	0.67	0.67	1
$\hat{Q}_7^*$	1.06	1.01	1	N/A
	$\hat{Q}_4$	$\hat{Q}_5$	$\hat{Q}_6$	$\hat{Q}_7$
(b)				
$\hat{Q}_4$	1			
$\hat{Q}_5$	0.97	1		
$\hat{Q}_6$	0.83	0.85	1	
$\hat{Q}_7$	0.51	0.56	0.56	1
$\hat{Q}_7^*$	0.85	0.88	0.92	N/A
	$\hat{Q}_4$	$\hat{Q}_5$	$\hat{Q}_6$	$\hat{Q}_7$
(c)				
$\hat{Q}_4$	1			
$\hat{Q}_5$	1.05	1		
$\hat{Q}_6$	1.02	0.98	1	
$\hat{Q}_7$	0.59	0.57	0.57	1
$\hat{Q}_7^*$	1.07	0.98	1	N/A
	$\hat{Q}_4$	$\hat{Q}_5$	$\hat{Q}_6$	$\hat{Q}_7$
(d)				
$\hat{Q}_4$	1			
$\hat{Q}_5$	1.13	1		
$\hat{Q}_6$	0.94	0.97	1	
$\hat{Q}_7$	0.54	0.62	0.57	1
$\hat{Q}_7^*$	0.99	1.1	1.07	N/A
	$\hat{Q}_4$	$\hat{Q}_5$	$\hat{Q}_6$	$\hat{Q}_7$

5.2. Application of metrics to experimental data

The proposed metrics have significantly closer correlations for primary impact points than secondary. This may be due to the response at the latter impact still including oscillations from the former, i.e. the desired measurement is buried in prior responses. For a real vehicle system, this problem is magnified, where there are more clearances and many more torsional modes. To illustrate, Fig. 11 provides sample data from experimental measurements of transient impacts in a torsional system. This experiment has been described in Ref. [3]. In this particular experiment the driveline sub-system of a powertrain test rig is excited in free vibration by releasing a preload applied at the tires. The modified system responds with oscillations in the lowest torsional mode (approximately 1 Hz for the driveline subsystem). During each cycle, the meshing final drive gears, splines and joints pass through clearance and impact. Fig. 11a provides normalized angular strain (torque), measured in the left and right axles and propeller shaft. The entire time history is not shown (see Ref. [3] for more details or similar results), rather the results are windowed around a time period of interest. The flat section showing zero strain is where the system is in clearance. Corresponding to these regions are impacts which have been measured (Fig. 11b) with an accelerometer fixed to the final drive housing near the pinion bearing. What is clear is that it is difficult to determine the exact impact times of all colliding bodies. Given a time lag in the system, one contacting pair will separate before another; likewise for impact and thus the responses are staggered. This generates a more complex data set to work with, as opposed to the

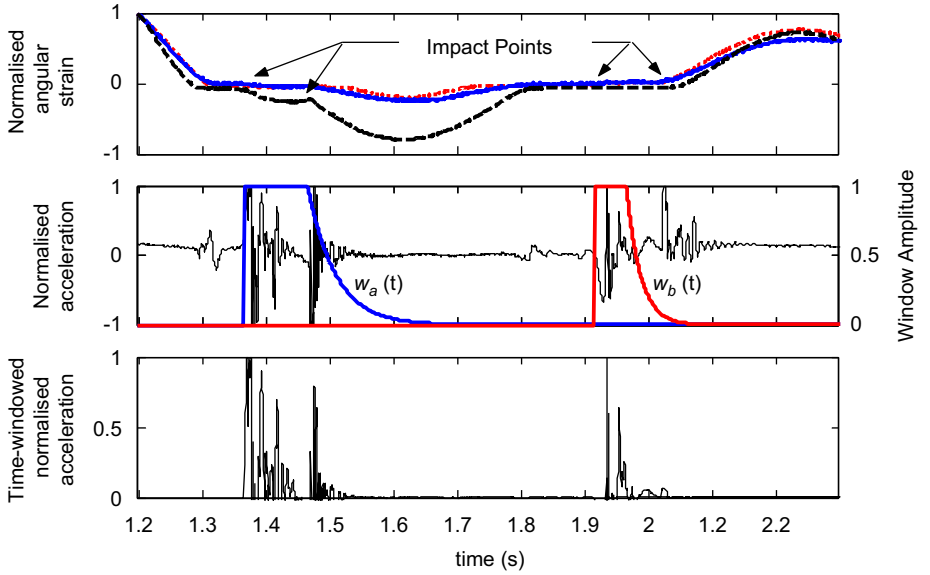

Fig. 11. Measured data for impacts in an experimental torsional system with clearances (vehicle driveline): (a) angular strain (dotted—right axle, solid—left axle, dashed—propeller shaft); (b) translational acceleration on final drive housing near pinion bearing and time-window functions; (c) squared time-windowed translation acceleration; (all magnitudes have been normalized to give a unity maximum).

simulation results shown for the system of Fig. 2. Consequently the utility of the time-windowed mean square acceleration metric becomes apparent. Determining where to measure peak to peak responses or initial rise is difficult, however by applying the time window (as shown in Fig. 11b as $w_a(t)$ and $w_b(t)$) the 'energy' over a given duration can be quantified. The two time windows illustrate the difference in selection of window lengths, obviously the analyst must judiciously make this selection. Fig. 11c shows the corresponding normalized time-windowed mean square accelerations.

In these experimental results, the occurrence of secondary impacts is not confirmed. This phenomenon, if it occurs, would be difficult to capture without a deliberate experiment with a single clearance, under controlled conditions and with appropriate torsional instrumentation. However, the experimental results do lead to this possibility, considering the number of acceleration spikes around each region of impacts. Future experimental work should consider such issues.

5.3. Simulation of torsional system with two clearances

Consider now the results of Fig. 12 where a second lash has been included in the generic torsional system, at location k_{45}, as shown in Fig. 2, with $\delta_{45} = 0.005$ rad. The simulation parameters are the same as for those of Figs. 5a and b ($T_m = 120$ Nm, $\Delta T_m = -T_m/1.4$). The acceleration responses are larger and there are also more impulses. In fact, for k_{23}, the primary impact at point d occurs at $t = 0.06978$ s, followed by secondary impacts at $t = 0.0727$ s and $t = 0.07642$ s and similarly for k_{45} at $t = 0.07293$ s(primary), $t = 0.07739$ s and $t = 0.08062$ s (secondary). The first clearance,δ_{23}, is leading the responses and each impact event, at either clearance element, causes impulses in the angular accelerations at both $\ddot{\theta}_3$ and $\ddot{\theta}_4$. Thus the response after the primary impact at d requires measurement of six impulses and again the utility of a time-windowed metric can be seen. A response at $\ddot{\theta}_3$ from an impact across δ_{45} will naturally include system lag, through k_{34} and visa versa. Following point g there are even more impulses. Relating back to the experimental results of Fig. 11b it is evident that there are many impulses. Though there are many clearances in that system, the measured responses may be characteristic of both multiple primary and secondary impacts, as observed in simulation data.

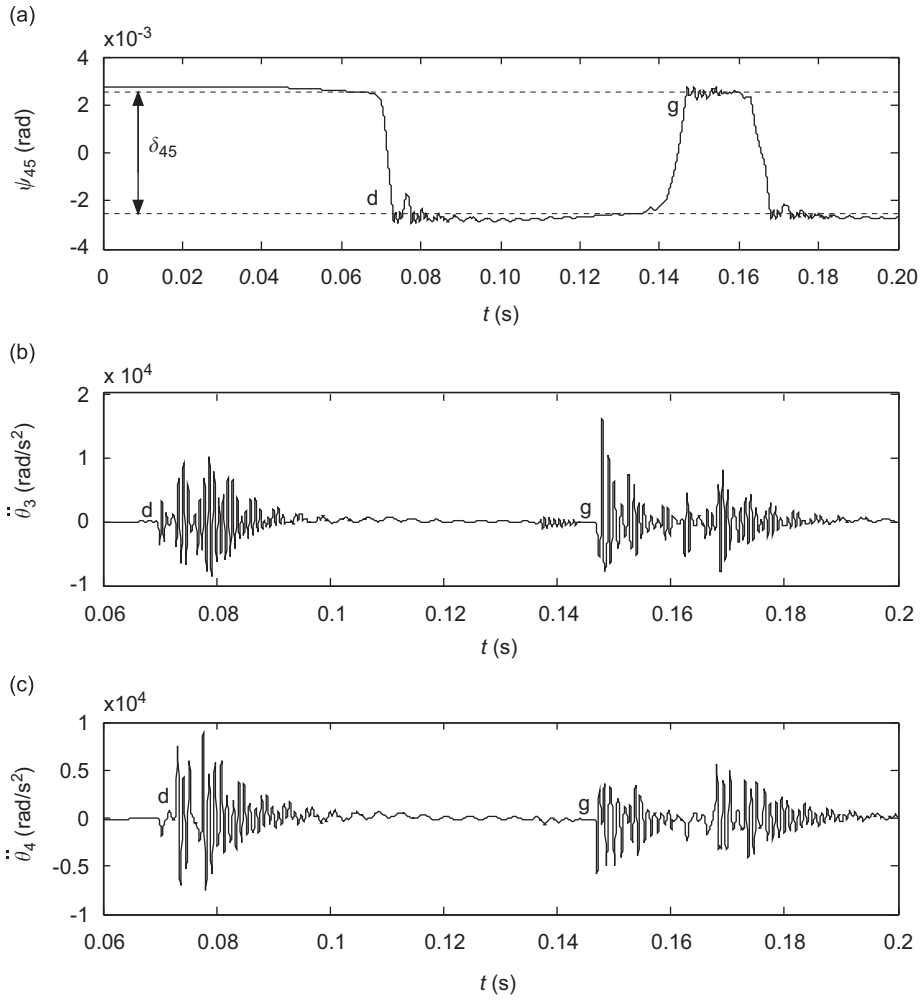

Fig. 12. Numerical results for torsional system with two clearances with excitation parameters $T_m = 120\,\text{Nm}$, $\Delta T_m = -T_m/1.4$, $t_a = 0.025\,\text{s}$, $t_b = 0.075\,\text{s}$, $\tau = 0.05\,\text{s}$: (a) relative angular displacement, $\psi_{45} = \theta_4 - \theta_5$, across nonlinear stiffness element, k_{45} (b) angular acceleration, $\ddot{\theta}_3$ with $\{0.06 \leqslant t \leqslant 0.2\}$; (c) angular acceleration,$\ddot{\theta}_4$ with $\{0.06 \leqslant t \leqslant 0.2\}$.

5.4. Effect of transient excitations

Referring to the surface maps of Figs. 9c–f, the severity of the impulsive response is clearly a non-monotonic function of $\mathbf{T}_m$ and $\Delta\mathbf{T}_m$. For initial primary impacts (point *d*), larger response magnitudes, whether measured by Q_4, Q_5, Q_6 or Q_7 correspond with larger $\mathbf{T}_m$ or $\Delta\mathbf{T}_m$, within the bounds of $\bar{\mathbf{M}}$. From another viewpoint, the magnitude of response is both a function of the impact time with respect to phase of the transient vibration at the lowest mode and the magnitude of this transient. If we were to assume that the time spent in clearance to be of very short duration compared to a period of this transient, then the separation and impact times could be considered to be the same with respect to the motions shown in Fig. 3a; these times are the points of zero crossing for the linear system. If the zero crossing is near a trough or a peak in this motion then the impact may be expected to be less severe. Note that this transient is not a pure decaying sinusoid until the ramp-down is complete and thus ramp-down time also is significant. Future work should examine impact response magnitudes versus the phase at zero crossings for both ramp-down and ramp-up transients. The relationship of response versus $\mathbf{T}_m$ and $\Delta\mathbf{T}_m$ is not as clear for the secondary impact at point *e*. Taking for example Fig. 9j for Q_6, peak to peak acceleration, the largest response occurs within $\{\mathbf{T}_m/1.1 \leqslant \Delta\mathbf{T}_m \leqslant 1.1\mathbf{T}_m\}$, tending towards $\Delta\mathbf{T}_m = \mathbf{T}_m/1.1$ as $\mathbf{T}_m$ increases. This difference to point *d* will be explained in the next section.

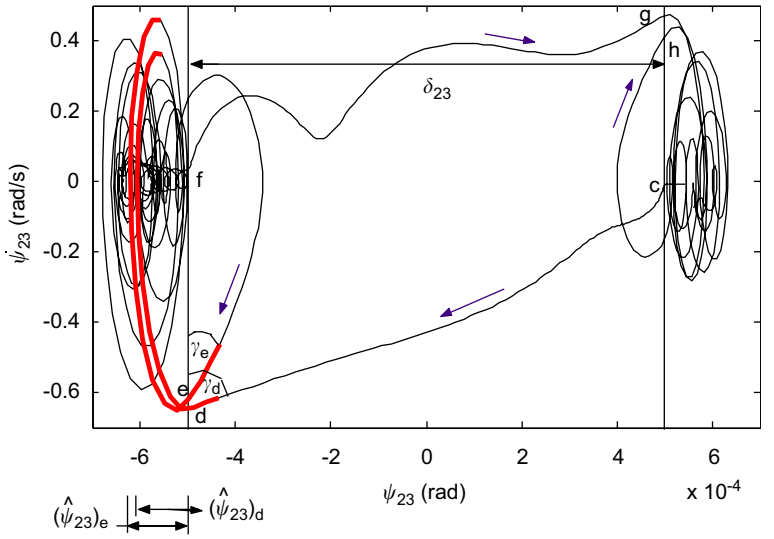

Fig. 13. Relative motion phase plane for impulse response simulation for $\{0.07<t<0.14\}$ with excitation parameters $T_m = 80\,\text{Nm}$, $\Delta T_m = -T_m$, $t_a = 0.025\,\text{s}$, $t_b = 0.075\,\text{s}$, $\tau = 0.05\,\text{s}$. Here the thickened line shows the solution flow through point d (primary impact) and point e (secondary impact) and corresponding $\hat{\psi}$ values.

6. Phase plane analysis

The following questions arise from the metric studies of Section 5: (1) Why do secondary impacts often cause a greater impulsive response than primary impacts? (2) Why does the relative kinetic energy just before an impact, Q_2, not equate with metrics measured after impact? (3) How does the relative acceleration, Q_3, play a part? To address these, we propose phase plane analyses as discussed next.

Recalling that $\psi_{23} = \theta_2 - \theta_3$, we define $\mathbf{\Pi}(t) = \begin{bmatrix} \psi_{23}(t) & \dot{\psi}_{23}(t) \end{bmatrix}$ as the phase plane solution for relative motion across the nonlinear stiffness element, k_{23}. Fig. 13 depicts a sample $\mathbf{\Pi}$ for the simulation of Section 3.3. The clearance region, δ_{23}, is indicated and the points of interest corresponding to Figs. 3 and 4 are shown as follows: points c and f, entering clearance; point d and g, primary impacts; point e and h, secondary impacts. The thickened lines show the solution flow through points d and e and past the point of maximum twist of the stiffness element from the initial impulse, which we define as $\hat{\psi}_{23}$. In this instance, $|(\dot{\psi}_{23})_d| > |(\psi_{23}(t) \quad \dot{\psi}_{23}(t))_e|$, so there is greater relative kinetic energy just prior to the primary impact, i.e. $(Q_2)_d > (Q_2)_e$. In fact for all $\bar{\mathbf{M}}$, by using the surface maps we see that $(\mathbf{S}_2)_d > (\mathbf{S}_2)_e$ except at one point, $\bar{M}_{1,1}$. Yet, as is clear from Fig. 13, $(\hat{\dot{\psi}}_{23})_e > (\hat{\dot{\psi}}_{23})_d$, and in this case the impulsive response is actually greater for the secondary impact. Note that this parameter is directly related to metrics measured immediately after impact, in that, for $\bar{M}_{3,5}$, $(Q_q)_e > (Q_q)_d$ ($q = 4,5$ and 6) and $(Q_7^*)_e > (Q_7^*)_d$. This is not the case for the whole surface, i.e. $(\mathbf{S}_2)_d$ does not exceed $(\mathbf{S}_2)_e$ for all j and k. This finding leads to some answers to the above-mentioned questions. If we were to assume that $(\dot{\psi}_{23})_d \approx (\dot{\psi}_{23})_e$, the key difference in the two events is the angle, γ_p, between the tangent to $\mathbf{\Pi}$ at the impact point and the clearance boundary. Hence an explanation may be found by examining solutions where $(\dot{\psi}_{23})_d$ is constant and γ_p is varied. To achieve this, we simulate the linear sub-system A impacting with sub-system B under controlled conditions. Fig. 14 demonstrates this concept. In each case the initial conditions are determined for $\mathbf{\Pi}(0)$ defined at a point within clearance and relative velocity upon impact specified as $(\dot{\psi}_{23})_d = -1$. The initial relative acceleration, $\ddot{\psi}_{23}(0)$, relates to γ_d, if determined for a constant value until impact, i.e. for $\{0t<t_d\}$. At $t = 0$ sub-system B is defined as motionless, $\theta_3(0) = \theta_4(0) = \theta_5(0) = 0$and $\dot{\theta}_3(0) = \dot{\theta}_4(0) = \dot{\theta}_5(0) = 0$ for all s. Sub-system A is driven by a constant torque, T_e. Introduction of parameters,

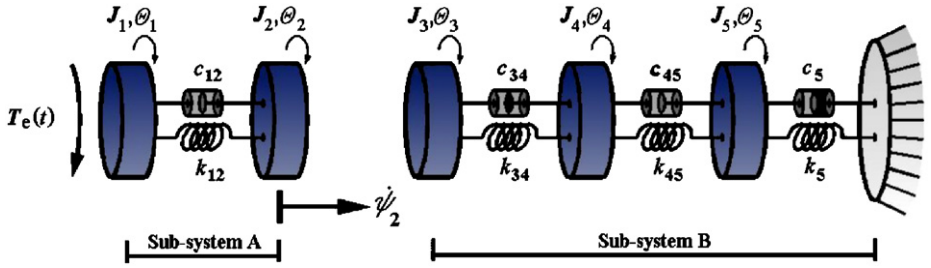

Fig. 14. Initial condition for phase plane analysis of controlled impact between sub-systems A and B.

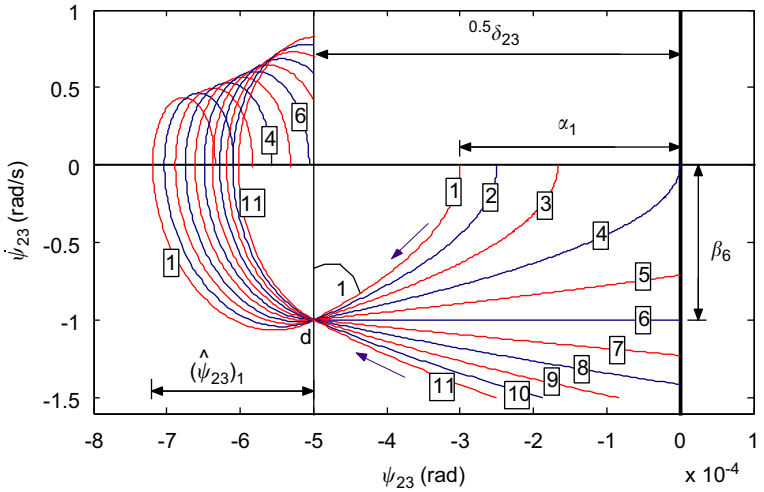

Fig. 15. Relative motion phase plane for controlled impacts between linear sub-system A and B as per Fig. 14. For each case, $\Pi(0) = [\alpha_s \quad \beta_s]$, $(\dot{\psi}_{23})_d = -1$ and $(\hat{\dot{\psi}}_{23})_s$ varies with defined values for $(\ddot{\psi}_{23}(0))_s$. See Table 5 for results summary.

Table 5
Summary of results for controlled impacts between linear sub-systems A and B as per Fig. 14

Case, j	α (rad)	β (rad/s)	$\ddot{\psi}_{23}(0)$ (rad/s^2)	T_e (Nm)	$\hat{\dot{\psi}}_{23}$ (rad)	γ (°)	γ*(°)
1	3.000E−04	0	−2500	−625	−1.219E−03	0.0229	49.0
2	2.500E−04	0	−2000	−500	−1.204E−03	0.0286	55.2
3	1.667E−04	0	−1500	−375	−1.189E−03	0.0379	62.4
4	0	0	−1000	−250	−1.175E−03	0.0572	70.9
5	0	−0.707	−500	−125	−1.162E−03	0.1140	80.1
6	0	−1.000	0	0	−1.149E−03	90.0000	90.0
7	0	−1.225	500	125	−1.138E−03	179.8888	100.1
8	0	−1.414	1000	250	−1.128E−03	179.9431	109.2
9	8.333E−05	−1.500	1500	375	−1.119E−03	179.9621	117.6
10	1.875E−04	−1.500	2000	500	−1.110E−03	179.9716	124.9
11	2.500E−04	−1.500	2500	625	−1.103E−03	179.9772	131.1

Note that γ denotes the real angle shown in Fig. 15, while γ* denotes the 'as seen' angle given the axis scaling of the figure.

$\alpha_s = (\psi_{23}(0))_s$ and $\beta_s = (\dot{\psi}_{23}(0))_s$, such that $(\mathbf{\Pi}(0))_s = [\alpha_s \ \beta_s]$ where s is the case index, yields:

$$(\ddot{\psi}_{23}(0))_s = \frac{-(\dot{\psi}_{23})_d^2 + \beta_s^2}{\delta_{23} - 2\alpha_s}. \tag{20}$$

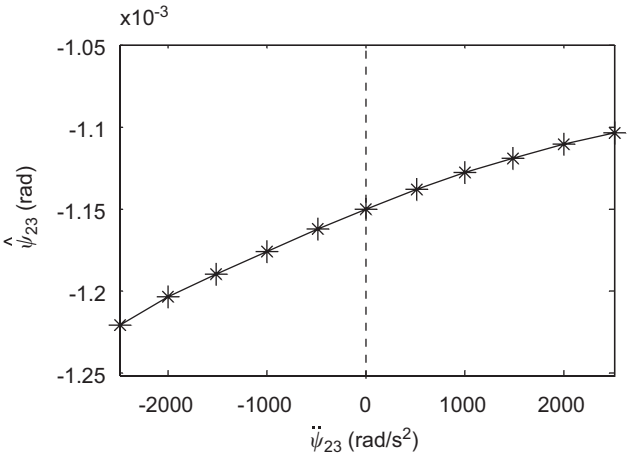

Fig. 16. Correlation between $\hat{\psi}_{23}$ and $\ddot{\psi}_{23}(0)$ for controlled impacts between linear sub-systems A and B as per Fig. 14. See Table 5 for results summary.

Hence the initial torque is $(T_e)_s = (J_1 + J_2)(\ddot{\psi}_{23}(0))_s$ and to ensure only rigid body motion of sub-system A, $(\theta_1(0))_s = [(T_e)_s - J_1(\ddot{\psi}_{23})_s/k_{12}] - \alpha_s$, $(\theta_2(0))_s = -\alpha_s$ and $(\dot{\theta}_1(0))_s = (\dot{\theta}_2(0))_s = \beta_s$. With this initial value formulation and by proper selection of α and β values, the desired flow of $\mathbf{\Pi}$ is achieved. The torque from the damping term, c_{23}, has been ignored in this formulation as its effect on $\ddot{\psi}_{23}$ for $\{0t < t_d\}$ is small.

Fig. 15 provides the results for parameter selection of Table 5. The maximum time resolution was refined to $\Delta t_{\max} = 4 \times 10^{-6}$ s ensuring greater accuracy in predicting $\dot{\psi}_{23}(t_d) = -1$. Parameters α_s, β_s, γ_s and $(\hat{\psi}_{23})_s$ are illustrated in Fig. 15 for various s values. By design, the impacts are in the same quadrant of the phase plane space as point d in Fig. 13. Through cases $s = 1$ to 11, the relative acceleration increases from $\ddot{\psi}_{23}(0t < t_d) = -2500$ to $\ddot{\psi}_{23}(0t < t_d) = 2500$ in 500 rad/s^2 increments; the driving torque corresponds as it is a multiple of $\ddot{\psi}_{23}(0)$. The variation in the quantifying parameter, $\hat{\psi}_{23}$, is determined solely by this acceleration, given that for each case$(\dot{\psi}_{23})_d = -1$, or $(Q_2)_d = 0.5(Q_2)(\dot{\psi}_{23})_d^2 = 0.125$. How this relates to γ is clear from Fig. 15 as a smaller γ gives larger response and visa versa. Note that in Table 5, γ is determined from actual values and seems an odd progression unless you compare the magnitudes of $\psi_{23}(t)$ and $\dot{\psi}_{23}(t)$; hence $\gamma*$ is provided as the 'as seen' angle in Fig. 15. The relationship between $(\ddot{\psi}_{23})_d$ and $(\hat{\psi}_{23})_s$ is shown in Fig. 16. Sub-system A accelerates into impact for $(\ddot{\psi}_{23})_d < 0$, when approaching the boundary, $\psi_{23} = -\delta/2$. But it decelerates for $(\ddot{\psi}_{23})_d > 0$. Visa versa for boundary $\psi_{23} = \delta/2$. As is evident from the $(\ddot{\psi}_{23})_d$ versus $(\hat{\psi}_{23})_s$ plot, the acceleration case is analogous to torque 'pushing' with the part of the impact response governed by momentum continuity and the deceleration 'pulling' against it.

From this analysis the propounded questions are answered. For the first question, the primary impacts tend to take a path in the phase plane such as shown for cases $s = 5$, 6 and 7, while secondary impacts take paths similar to case $s = 1$ or 2. Referring to Figs. 3, 4 and 13 this is clearly the case for over much of the simulation domain for $\bar{M}_{3,5}$. Similarly so for most impact cases within $\bar{\mathbf{M}}$. Hence, secondary impacts often have the greater impulse response. Each particular case depends on the relative kinetic energy immediately prior to impact and relative acceleration, which answers the second and third questions. The metric Q_2 does not take the acceleration into account, hence it could be an ineffective index for vibro-impacts. For the phase plane study, $(\ddot{\psi}_{23})_d$ was governed by constant T_e; however, for simulation study using $\bar{\mathbf{M}}$, T_e is a function of time and affects $(\ddot{\psi}_{23})_p$, whether at $p = d$ or e, or another impact point. Also $(\ddot{\psi}_{23})_d$ is largely dependent on vibration response of the whole system and the entire transient nonlinear behavior prior to that point. Hence a further refinement of Q_2 to account for f is impractical.

7. Conclusion

Chief contributions of this research include better quantification and an understanding of impulsive responses in torsional systems with clearances that occur during rapid changes in external torque excitations.

The torsional system we formulated is related to a vehicle driveline as it replicates basic modal properties at low, mid and high frequencies. A map of external torque excitations is defined to cover a range of external torque excitations typical to such a system. Then nonlinear transient solutions are found numerically for the entire excitation map including a single clearance. Convergence of such simulations is studied carefully for variations in solver tolerance and maximum time step for the utilized variable stepping algorithm. Seven metrics are proposed (including a few previously identified by prior researchers) for the quantification of the impulsive response. These include a global metric that indicates the number and nature of impacts, metrics measured just before impact, the relative kinetic energy and relative acceleration of impacting bodies, metrics measured just after impact, initial torque rise, initial velocity rise, peak to peak acceleration and time-windowed mean-square acceleration. Six metrics are evaluated against each other via surface maps and line plots. Impacts are defined as primary when they occur after crossing over the entire clearance and secondary when they follow a rebound into clearance after a primary impact. Phase plane analysis is applied to explain the differences between the magnitudes of impulses for impact types, illustrating that the relative acceleration between impacting bodies and their relative kinetic energy determine their severity. Analysis shows that the metrics measured after impact correlate well and thus metrics based on the kinetic energy of bodies just prior to the impact could be invalid. Nonetheless, as the number of clearances and number of secondary impacts increase, the motions become too complicated for simplistic initial rise or peak to peak measurements to be effective quantifiers. Thereby the utility of the time-windowed mean-square acceleration metric is evident. Using numerical or experimental data sets for systems with multiple clearances, it is shown how this metric permits an 'energy' calculation with multiple impact events that could be either isolated or combined.

In spite of the above-mentioned studies, several unresolved research issues still remain. Some topics for future work include the following: Quantification of the magnitude of impulsive response as a function of phase of transient vibration within the envelope of linear system solution; a better understanding the significance of the location of clearances and the effect of multiple clearances; detailed experimental studies under controlled excitations; development of time domain transfer path techniques; psychoacoustic perception of impulses and the like. Finally, an effort should be made to develop a semi-analytical method that would synthesize time domain characteristics of sub-systems.

References

[1] J. Wang, R. Li, X. Peng, Survey of nonlinear vibration of gear transmission systems, *Applied Mechanics Review* 56 (3) (2003) 309–329.
[2] D.A. Gilbert, M.F. O'Leary, J.S. Rayce, Integrating test and analytical methods for the quantification and identification of manual transmission driveline clunk, *SAE Technical Paper* 2001-01-1502, 2001.
[3] A. Crowther, R. Singh, N. Zhang, C. Chapman, Impulsive response of an automatic transmission system with multiple clearances: formulation, simulation and experiment, *Journal of Sound and Vibration*, in press, doi:10.1016/j.jsv.2007.05.053.
[4] W. Oh, R. Singh, Examination of clunk phenomena using a non-linear torsional model of a front-wheel drive vehicle with manual transmission, *2005 SAE Noise and Vibration Conference*, Traverse City MI, May 16–19 2005, SAE Paper 2005-01-2291.
[5] S. Dubowsky, F. Freudenstein, Dynmic analysis of mechanical systems with clearances, part 1: formulation of dynamic model, *Transactions of the ASME Journal of Engineering for Industry* (1971) 305–309.
[6] S. Dubowsky, F. Freudenstein, Dynamic analysis of mechanical systems with clearances, part 2: dynamic response, *Transactions of the ASME Journal of Engineering for Industry* (1971) 310–316.
[7] G.W. Blankenship, A. Kahraman, Steady state forced response of a mechanical oscillator with combined parametric excitation and clearance type non-linearity, *Journal of Sound and Vibration* 185 (1995) 743–765.
[8] S.W. Shaw, P.J. Holmes, A periodically forced piecewise linear oscillator, *Journal of Sound and Vibration* 90 (1983) 129–155.
[9] W. Goldsmith, *Impact: The Theory and Physical Behavior of Colliding Solids*, E. Arnold, London, 1960.
[10] R.M. Brach, *Mechanical Impact Dynamics: Rigid Body Collisons*, Wiley, New York, 1991.
[11] W.J. Stronge, *Impact Mechanics*, Cambridge University Press, Cambridge, 2000.
[12] V. Babitsky, V.L. Krupenin, *Vibration of Strongly Nonlinear Discontinuous Systems*, Springer, New York, 2001.
[13] C. Padmanabhan, R. Singh, Influence of clutch design on the reduction and perception of automotive transmission rattle noise, *Proceedings of NOISE-CON 93*, May 2–5, Williamsburg, VA, 605–612. 1993.
[14] R. Krenz, Vehicle Response to Tip-in/Tip-out, *SAE Technical Paper* 850967, 1985.
[15] A. Crowther, N. Zhang, R. Singh, Development of a clunk simulation model for a rear wheel drive vehicle with automatic transmission, *2005 SAE Noise and Vibration Conference*, Traverse City MI, May 16–19 2005, SAE Technical Paper 2005-01-2292.
[16] K.H. Hunt, F.R.E. Crossley, Coefficient of restitution interpreted as damping in vibroimpact, transactions of the ASME, *Journal of Applied Mechanics* (1975) 440–445.

[17] T.C. Kim, T.E. Rook, R. Singh, Effect of nonlinear impact damping on the frequency response characteristics of a torsional system with clearance, *Journal of Sound and Vibration* 281 (3–5) (2005) 995–1021.
[18] T.C. Kim, T.E. Rook, R. Singh, Effect of smoothening functions on the frequency response of an oscillator with clearance non-linearity, *Journal of Sound and Vibration* 263 (3) (2003) 665–678.
[19] C. Padmanabhan, R.C. Barlow, T.E. Rook, R. Singh, Computational issues associated with gear rattle analysis, *ASME Journal of Mechanical Design* 117 (1995) 185–192.
[20] M. Kubur, A. Kahraman, D.M. Zini, K. Kienzle, Dynamic analysis of a multi-shaft helical gear transmission by finite elements: model and experiment, *ASME Journal of Vibrations and Acoustics* 126 (2004) 398–406.
[21] A. Kahraman, A.A. Kharazi, M. Umrani, A deformable body dynamic analysis of planetary gears with thin rims, *Journal of Sound and Vibration* 262 (2003) 752–768.
[22] M.T. Menday, H. Rahnejat, M. Ebrahimi, Clonk: an onomatopoeic response in torsional impact of automotive drivelines, *Journal of Automobile Engineering* 213 (1999) 349–357.
[23] A. Kahraman, G.W. Blankenship, Experiments on nonlinear dynamic behavior of an oscillator with clearance and periodically time-varying parameters, *Journal of Applied Mechanics* 64 (1997) 217–226.
[24] C. Yukel, A. Kahraman, Dynamic tooth loads of planetary gear sets having tooth profile wear, *Mechanism and Machine Theory* 39 (2004) 659–715.
[25] H. Vinayak, R. Singh, C. Padmanabhan, Linear dynamic analysis of multi-mesh transmissions containing external, rigid gears, *Journal of Sound and Vibration* 185 (1) (1995) 1–32.
[26] A.R. Crowther, N. Zhang, Torsional finite elements and non-linear numerical modelling in vehicle powertrain dynamics, *Journal of Sound and Vibration* 284 (3-5) (2005) 825–849.
[27] L.F. Shampine, M.W. Reichett, The Matlab ODE suite, *SIAM Journal of Scientific Computing* 18 (1997) 1–22.